

Muon Scattering Tomography: Utilizing Silicon Photomultiplier Arrays to Trilaterate Muon Multiple-Coulomb Scattering Events

Trevor Daino
Arpad Voros
Michael Kronovet

May 2017

Abstract

Muon scattering tomography is a passive imaging technique capable of creating detailed 3-D images, interpolating the elemental composition of materials in a scan field, and analyzing the structure of high-Z materials. Given that development of the technique is in a stage of relative novelty, very few of them are commercially used. The muon scattering tomography apparatuses currently operated at research institutions and companies are extremely cost-inefficient. In this experiment, the objective is to increase the cost-effectiveness of muon scattering tomography devices by localizing ionization events within solid state scintillators for optimal rendering of muon multiple-Coulomb scattering incidences. This design implements silicon photomultiplier arrays which summate Geiger-mode avalanche photodiode current discharge to trilaterate muon trajectory when sensing the light output from solid blocks of a polyvinyl toluene based organic scintillator. Operational amplifiers were utilized to adapt the digital read-out circuit towards low-amplitude and low-duration signal conversion. Additionally, sample and hold circuitry with automatic threshold-triggering were developed using discrete components as a cost-effective method of extenuating the analog signal modulation for minimal information loss during digital conversion. The calibration and assessment of the device's performance were segmented into three stages: analog signal analysis, digital trilateration, and muon detection. Afterwards, a Monte Carlo simulation was developed to determine the cost effectiveness and temporal efficiency of a scaled-up rendition of the device model. When scaled up, the device would be more cost effective for a variety of applications including carbon sequestration, cargo inspection, nuclear waste monitoring, mass transit security, and mining applications.

Contents

1 Introduction

1.1 Muon scattering tomography (MST)

1.2 Conventional MST designs

2 Design Parameters

2.1 Key specifications and goals of functionality

2.2 Engineering process

2.3 Novel aspects of approach

2.3.1 Trilateration

2.3.2 Prismatic scintillator geometry

2.3.3 Data acquisition and scan volume reconstruction

2.3.4 Increase of photon detection efficiency (PDE)

2.3.5 Scaled up rendition

3 Materials and Methods

3.1 Polyvinyl toluene based scintillator

3.2 Silicon photomultiplier array

3.3 Shielding

3.4 Electronics

3.4.1 Procedure

3.4.2 Signal processing

3.5 Monte Carlo procedure

3.5.1 Muon source generation

3.5.2 Muon propagation

3.5.3 Photomultiplier output model

4 Results

4.1 Calibration

4.2 Simulation

4.2.1 Electrical simulation

4.2.2 Monte Carlo simulation

4.2.2.1 Temporal efficiency

4.2.2.2 PDE

4.2.2.3 Voxel resolution

5 Conclusion

5.1 Cost efficiency

5.2 Temporal efficiency estimation

5.3 Performance comparison

5.4 Limitations in design

5.5 Further research

6 References

1 Introduction

Muon scattering tomography is a recently invented, passive imaging technique that measures the discrepancy of incoming and outgoing cosmic ray muon trajectories to generate 3-D tomographic images of materials. Muons are naturally occurring cosmic radiation, and they are the most prevalent high energy particle at sea level. The large mass of muons (207 times as massive as an electron) allow them to penetrate deep into Earth's surface.²⁷ Muons are minimally ionizing, so they are not significantly harmful to biological tissues. They interact with matter primarily through Coulombic interactions as opposed to those involving nuclear forces in the energy spectra above 100 MeV.

The figure immediately below depicts the typical air shower of an iron nucleus in the thermosphere which results in muon production from pion decays as a form of secondary particle formation, and the next figure below depicts a generalized schematic which segments secondary shower production into electromagnetic, mesonic, and nucleonic components.

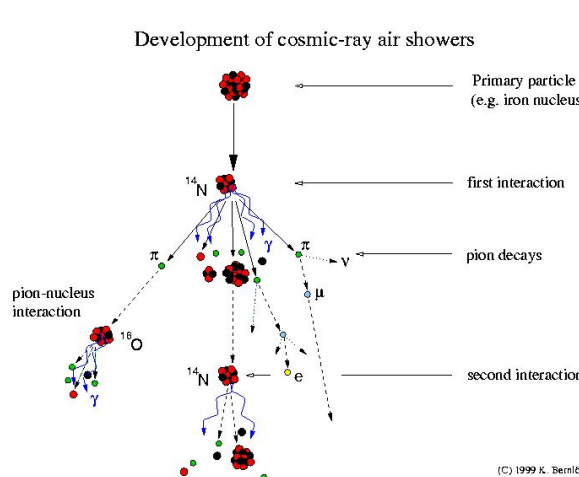


Figure 1.1³³

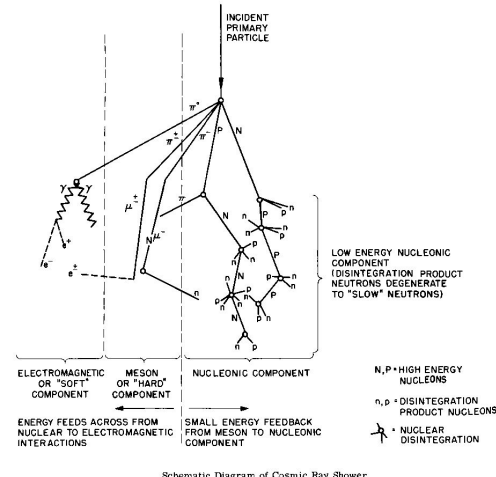


Figure 1.2⁶

The scattering exhibited by a muon through a material, typically with a high mean Z (atomic number), follows approximately a Gaussian distribution centered at zero radians and with a standard deviation that scales with the radiation length inherent to the material. Muons possess a mean decay time of 2.2 microseconds and due to time dilation effects they are able to permeate the atmosphere from their site of generation and penetrate tens of meters into the lithosphere.²⁷ The angular distribution of the cosmic ray muon flux is approximately proportional to the square of the cosine of the solar zenith angle.³¹

$$\frac{dI}{d\theta} = \frac{d}{d\theta} [\cos^2(\theta)][I_0]$$

The muon flux at sea level with a desirable energy spectra angular distribution is about 1 muon per square centimeter per minute, and the majority of sea-level flux muons comprises of those with momenta between 100 MeV/c and 100 GeV/c.²⁷ At this level of momentum, muons exhibit a minimally ionizing behaviour when traversing material. The muon's exceptionally high attenuation length through various material cross

sections coupled with its ability to undergo multiple-Coulomb scattering makes it an ideal candidate for tomographic imaging of mid- to high-Z materials.

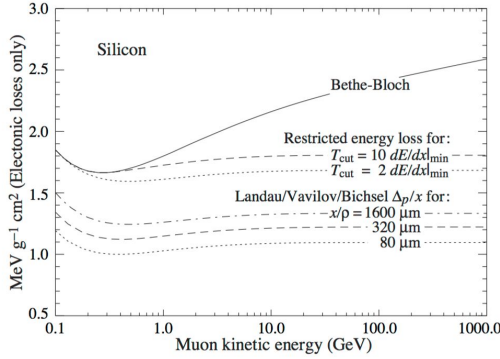


Figure 1.3⁶

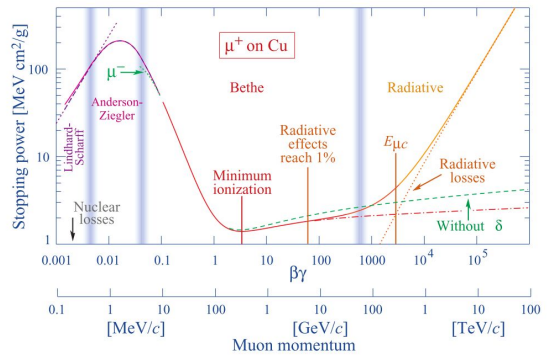


Figure 1.4⁶

The left figure shows electronic losses in muon kinetic energy per the initial kinetic energy of a muon as it penetrates a silicon cross-section. It can be observed that the minimally-ionizing properties of muon-matter interaction is not fully encapsulated by the Bethe-Bloch paradigm of lepton propagation through matter. The behavior of muons in this regard is more aptly described by the Landau-Vavilov model with the Bischel density effect correction, because this treats the parameterization of muon ionization events as part of a non-Gaussian probability density function. The figure on the right is a plot of the stopping power (energy loss per quantized material cross-section) per the spectrum of incident muon momentum. It can be seen that in the cosmic ray muon momenta interval (aforementioned), the minimum ionization point (in this depiction for copper, but most materials are also in the interval between 100 MeV/c and 800 MeV/c) is included, up to about the point where radiative energy loss effects exceed 1 percent of the total losses exhibited.

1.1 Muon scattering tomography (MST)

There are currently a wide variety of applications for muon tomography, with many uses still being realized. Specifically, muon tomography is very useful for detecting nuclear and radioactive sources. This aspect of muon tomography is used to expose potential threats such as nuclear weapons in cargo, to prevent radioactive sources from being recycled along with scrap metal in power plants, and to monitor the nuclear decay products in damaged reactor cores. In Japan, researchers accurately used muon tomography to inspect the damage to the Fukushima Daiichi nuclear reactor cores resulting from Japan's massive earthquake and tsunami in 2011.¹⁸ The high scattering angle of muons when coming in contact with such nuclear and radioactive materials make muon tomography ideal for scoping out high-Z materials. In addition, muons are able to penetrate through dense and high depth shielding which make them optimal for detecting concealed threats. There are many applications of muon tomography to be explored in greater detail such as geological surveying, mass transit security, measuring the stability of buildings and bridges, or even the functionality of an old furnace. Some muon tomography devices are useful looking at very small biological materials that are past the prior to the limit of optical diffraction. Muon tomography can also be utilized to identify radioactive sources amidst other materials that typical gamma ray detectors could interfere with. One

application of muon tomography that will most likely be further explored in the near future is carbon sequestration. This relatively new concept helps prevent the harmful effects of fossil fuels by depositing CO₂ emissions from power stations underground. Muon tomography can be used to continuously monitor the density of the rocks in these carbon deposits deep underground, making the process of carbon sequestration much safer.

1.2 Conventional MST designs

Muon scattering tomography is in a stage of relative novelty, and the apparatuses currently operated at research institutions are extremely expensive and (are very inefficient relative to temporal and spatial resolution) have low volumetric pixel (voxel) resolution ($\geq 1 \text{ cm}^3$).

In 2003, when the first muon-scattering tomographical device was developed at the Los Alamos National Laboratory, drift chambers were used to determine particle position. Since this initial design, drift tubes have become the most conventionally technique for detecting muon instances. When the gas within the drift chamber is ionized, electron-ion pairs are formed which drift in the direction of the cathode and anode, respectively. Free electrons will furtherly ionize other gas molecules, creating a cascade effect that produces a measurable current in the vicinity of the particle incidence. This allows for extreme reliability and accuracy when determining particle positions. However, these drift tubes are exceedingly costly, require high maintenance, and use complex, costly readout electronics.

Optical fibres in a lattice formation coupled with scintillating material have been used in early forms of muon radiography, and there are some current implementations of this technique for building muon scattering tomography devices. Fibre optic cables cladded with scintillating material, when organized in a perpendicular lattice structure, sense particle instances through the coincidental emission of light at an intersecting node. Unfortunately, although the method is less extravagant than drift chambers, this adaptation of muon scattering tomography is moderately expensive due to the implementation of fibre optics and photomultiplier channels allocated per each fibre. There is also a substantial loss of volumetric pixel (voxel) resolution that arises from manufacturing limitations in the cross-sectional diameter of the fibres, and the overall architecture is difficult and strenuous to maintain.

2 Design Parameters

In an attempt to reduce the cost, improve accuracy, and develop a successful commercially available device for muon scattering tomography, a unique design which localized ionization events within solid state scintillators for optimal rendering of muon multiple-Coulomb scattering incidences was pursued. Silicon photomultiplier (SiPM) arrays, which summate Geiger-mode avalanche photodiode current discharge, were implemented to trilaterate muon trajectory when sensing the light output from volumetric polyvinyl toluene based organic scintillators. Substituting drift chambers for such long-decay scintillators coupled with SiPM arrays would significantly decrease cost while maintaining a similar voxel resolution.

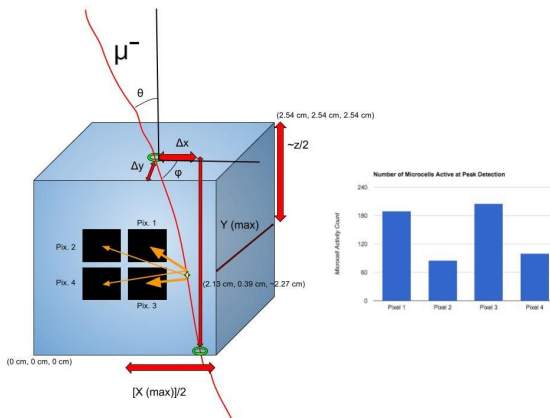


Figure 2.1

The plastic scintillator acts as a median of transformation; the particles incidence is converted into an optical signal with intensity relative to the amount of energy deposited within the sensing block. Solid-state photomultiplying sensors placed upon the plastic transform the optical signal to an electrical signal, with varying intensities allow for disparities in voltage in the processed electrical signal to be analysed. These disparities are quantitative inputs that may be interpreted (by being processed as inputs into the trilateration procedure) into spatial information regarding the position of the muon trajectory hypocenter. The discrete set of Cartesian coordinates collected from the four sensor modules enables the determination of an inbound and outbound trajectory from which a scattering angle may be derived as a three-dimensional reconstruction.

2.1 Key specifications and goals of functionality

The parameters of conducting muon scattering tomography with a static scan volume are concisely given by the metrics of temporal efficiency (defined as the total average time required for the multilateration algorithm to yield a specified threshold of certainty in estimating a voxel's mean material Z-value for a specified proportion of the total voxel population), voxel resolution (the physical dimensioning of the voxels in the volume reconstruction phase), and the cost of the device's implementation. It is the premise of the utilization of silicon photomultipliers and low-efficiency plastic scintillators in conjunction to conduct tomographic imaging with significant reduction in the overall monetary expenditure required for system manufacture.

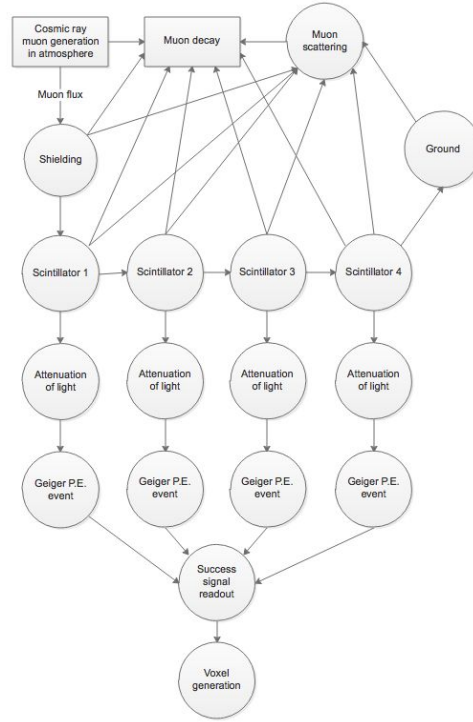


Figure 2.1.1

In the design of a novel approach to muon scattering tomography, the established goal is to make an improvement in one of the three aforementioned metrics while keeping the other two constant or altered by a lesser proportion than the metric being manipulated. As such, it is the set directive to reduce the overall cost of muon scattering tomography while maintaining an equitable voxel resolution and a modified temporal efficiency that does not exceed the proportional change in cost.

There are two quantitative factors that contribute to the notion of voxel resolution. The first, dependent on the total influx of photons into the SiPM over the duration of the scintillator emission, is that related to the probabilistic estimation of the multiple-Coulombic scattering angle of a singular muon incidence according to an approximated Gaussian distribution. The second is the physical dimensioning of individual voxels, which is dependent on both the total influx of photons and the microcell population of the SiPM “pixel” (CMOS microcell matrices).

The established goal for voxel resolution within any sized rendition of the volumetric scintillator and SiPM tomography concept is a thresholding for multiple-Coulombic scattering angle that enables the device to differentiate between two elements of the elements in the actinide series. Considering Np (93) and Pu (94) as a target benchmark for z-value discretion, the minimum detectable scattering angle would be determined by the following formula, which is dependent upon total microcell count, the cross-sectional area of the scintillator from the zenith perspective, and the scintillation efficiency.

$$\theta_{min} = \sin^{-1}(pI_0 \int_{\frac{-\tan^{-1}(\frac{d_{width}}{d_{scan}+d_{gap}+d_{depth}})}{2}}^{\frac{\tan^{-1}(\frac{d_{width}}{d_{scan}+d_{gap}+d_{depth}})}{2}} E_R(x) \cos^2(\theta) \frac{N_{microcell}[E]}{A_{cross}}),$$

where $I_0 = 0.007 \text{ cm}^{-2} \text{s}^{-1} \text{sr}^{-1}$.

The dependency of the above expression on the physical dimensioning of the scintillator is derived from a combination of attenuation and dispersion effects of light in the uncladded cubic-prototype model, and the probability of multiple muon events occurring within the span of optical signal decay. For the prototype outlined herein, the approximate scintillator decay constant is 285 ns. With this angular resolution, it is then possible to determine the volumetric constraints for partitioning the scan volume into discrete compartments, or as voxels in the software-based interpretation of scan volume data.

2.2 Engineering process

Prior to contemplating the use of SiPM arrays and scintillators to detect muons, a different design utilizing scintillating fibres was pursued. Scintillating fibers were to be assembled in a lattice structure with individual photodiodes on 2 adjacent sides of the grid. The benefits of this were a reduction cost from the conventional drift chamber method. The main deterrent of this approach was the poor voxel resolution (delimited by the physical diameter of the cables, to 5 mm), which resulted in significant size constraints for building a functioning prototype with discernable results. In order for the device to successfully discern between the 0.015 radian mean difference in Coulombic scattering angle, the total separation between the first and last scintillating fibre lattices would have to be in slight excess of 3 meters. It was implausible to construct such a large prototype model with our limited resources.

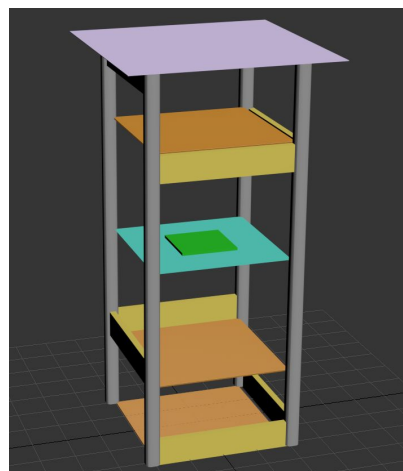


Figure 2.2.1

After realizing the futility of the previous approach, a novel, low cost method was designed and considered: utilizing SiPM arrays by volumetric scintillators to detect average muon position via trilateration. This strategy for finding muon position was a completely novel idea, therefore construction and implementation was arduous with no prior direction to follow. The new design had a resulting voxel resolution on par with

that of drift tubes. Therefore, it was logical to pursue and build a scaled-down prototype model in order to prove the efficacy of the new system.

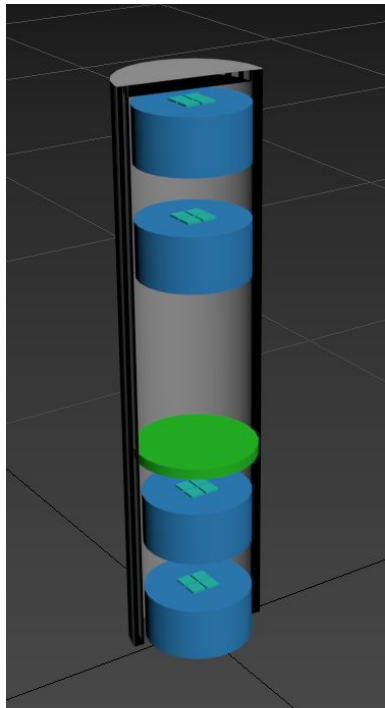


Figure 2.2.2

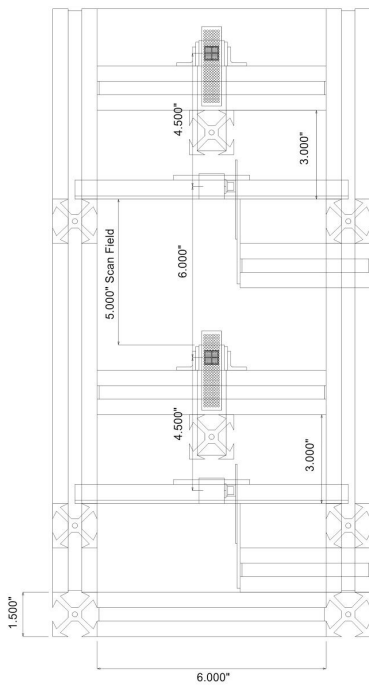


Figure 2.2.3

Constant modifications were made when problems or improved alternatives were identified. For example, when building the prototype, SiPM arrays were placed on the sides of scintillator instead of on top to prevent the SiPM arrays' electric fields from interfering with the scattering of the muons. Eventually, a flaw was discovered in the trilateration design when trying to scale the design up to fit real world applications. Approximately 0.58 percent of the light emitted from the scintillator was to be received by an individual SiPM pixel, making it difficult to discern between thermal noise and a muon instance. A parabolic optical cavity system with increased photon detection efficiency (PDE) was considered in accordance with a scaled up model in order to remedy the issue.

2.3 Novel aspects of approach

2.3.1 Trilateration

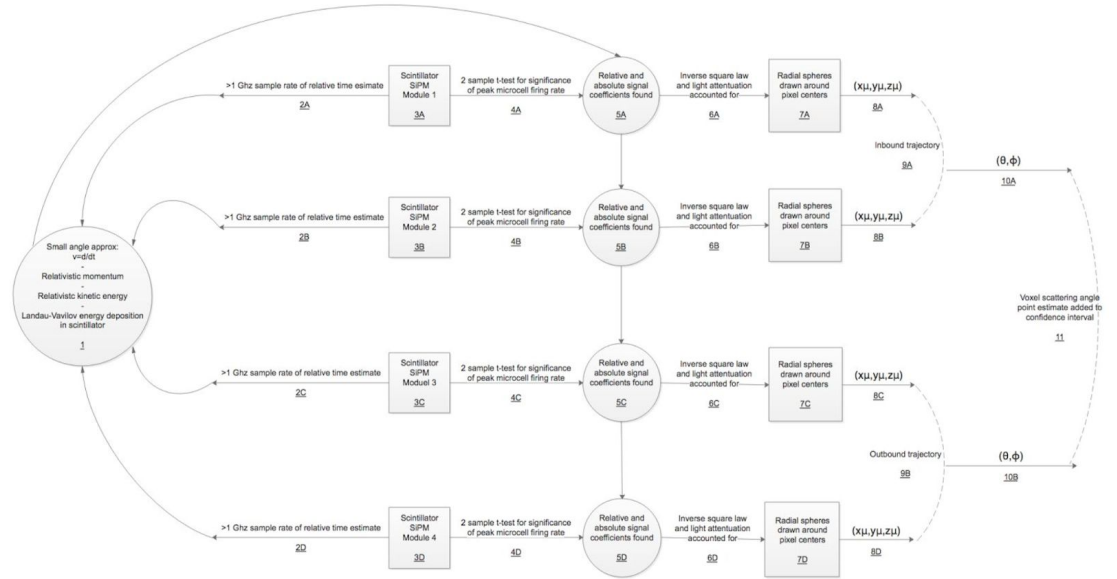


Figure 2.3.1.1

Calculating the hypocenter within each scintillator will allow determination of trajectory by tabulating the slope of muon interactions within the first two scintillators and then comparing it to the slope detected from the last 2 scintillators, after the muon changed trajectory. Our trilateration algorithm involves determining the muon momentum using a timing system with a Schmitt trigger (see [3.4.2]) situated at the output of each photomultiplier array. Once the muon momentum is known the radius of a virtual sphere projected about the center of each SiPM can be found when taking into account the inverse square law for the expansion of the photosphere and attenuation effects inside the scintillator. Energy deposition in scintillator is stochastically computed by using a Gaussian fit to the Landau-Vavilov distribution, and using the mode as a point estimate. Absolute optical intensity indicates depth of muon trajectory hypocenter into the volume of the scintillator, perpendicular from planar face of photomultiplier array. This takes into account the inverse square law of light sphere dispersion, attenuation effects in solid-state scintillator material, and empirical optical yield of the scintillator (Birk's Law). The consummate equation for determining the Cartesian coordinates of muon hypocenters in a scintillator with a known array of Geiger discharge outputs is stated below:

$$p = \frac{m_0(\frac{d}{t_{peak2} - t_{peak1}})}{\gamma}$$

$$E = \sqrt{(pc)^2 + (m_0c^2)^2}$$

$$\frac{dE}{dx} \rightarrow \Delta p = \xi [\ln \frac{2m_e c^2 \beta^2 \gamma^2}{I} + \ln \frac{\xi}{I} + 0.2 - \beta^2 - \delta]$$

$$I = x S \frac{\frac{dE}{dx} ad}{1 + k_B \frac{dE}{dx}} \frac{e^{-\mu x}}{\Omega |r|^2}$$

$$r_{p1}^2 = (16.3 - x_\mu)^2 + (y_\mu)^2 + (16.3 - z_\mu)^2$$

$$r_{p2}^2 = (5.6 - x_\mu)^2 + (y_\mu)^2 + (16.3 - z_\mu)^2$$

$$r_{p3}^2 = (16.3 - x_\mu)^2 + (y_\mu)^2 + (5.6 - z_\mu)^2$$

$$r_{p4}^2 = (5.6 - x_\mu)^2 + (y_\mu)^2 + (5.6 - z_\mu)^2$$

Relative optical intensity is determined by the discrepancy in Geiger discharge count between vertical and horizontal pairs of photomultiplier pixels indicates position of muon trajectory hypocenter along both dimensions of the planar surface where the photomultiplier array is placed. Combining absolute and relative optical intensity measurements from all four scintillating modules enables the determination of an inbound and outbound trajectory for a singular muon incidence, thereby finding the multiple-Coulomb scattering angle. Collusion between separate muon instances are avoided due to low ambient flux of cosmic ray muons and partitioning of the scintillating material (where each partition has a respective photomultiplier array).

The spacing between scintillators allows for the small angle approximation to be established regarding the zenith of incident muon trajectories. If the assumption is made that muons travel at a near vertical asymptote (minute scattering within the scintillator will always occur producing a deviation from the vertical) it is possible to measure the relative timing of scintillator ionization and resulting photomultiplier peak output. With this relative time the velocity of the muon can be determined and therefore its kinetic energy. Given that the energy of the muon combined with the design parameter of the scintillator maximizes the number of Coulombic interactions with a given sampling surface area, the actual energy deposited will be close to the mean described by the Landau-Vavilov distribution. The scintillation optical yield and surface flux distribution will be relatively consistent permitting the data acquisition system to calculate the distance between the center of the SiPM and the hypocenter of the muon path. Knowing the original muon momentum allows for the inverse square reduction in the light intensity per steradian of the light sphere emerging from each discrete origin of scintillation coupled with light attenuation effects to be accounted for. As a result, it is possible to ascertain an absolute Cartesian coordinate of the muon path hypocenter internal to the scintillator prism.

2.3.2 Prismatic scintillator geometry

The categorization of plastic scintillating materials tends to be characterized by relatively low scintillation efficiencies versus their inorganic counterparts. The primary advantage of opting to use plastic scintillator materials with wavelength shifting fluors is therefore that of minimizing cost. For the detection of minimally ionizing radiation, especially with the purpose of deriving a differential signal between SiPM outputs, the

path length which a muon incident intersects the scintillator should be maximized per the volume of the scintillating material. In the present design, cubic scintillator geometry was opted for because of its relative simplicity in manufacture and for its satisfactory volume to surface area ratio. Three of the faces on the scintillating cube were diamond-milled to yield transparent surfaces for optimum performance in the UV calibration stage (see [4.1]). Otherwise, the only transparent face required is that on which the silicon photomultiplier array is situated.

In the design addendum to the original cubic scintillator model, parabolic optical cavities with Bragg reflector claddings were conceptualized for a scaled-up implementation of the SiPM and prismatic scintillator tomography technique. Muon incidence trilateration would conducted by discerning angle of deflection along X- and Y- axis of the planar surface of the parabolic reflector cavity. This data also coupled with momentum determination and absolute scintillation intensity to find muon hypocenter distance from the center (maximized path length) according to Birk's Law.

2.3.3 Data acquisition and scan volume reconstruction

The data acquisition process must take into account each stochastic signal conversion stage inherent in the multilateration algorithm. These successive transfers of data exist first between muon kinetic energy to localized ionization within the scintillator volume, activation of fluorescing and wavelength-shifting compounds embedded in the scintillating substrate, regional photon emission, generation of a unique temporal exposure of optical flux on the surface of the scintillator, a directly proportional microcell firing rate (as long as the total optical intensity is not in excess of the SiPM's dynamic range). The combination of trilateration outputs for each scintillator during a muon incident yields an inbound and outbound trajectory, from which a scattering angle is interpreted and logged for the particular voxel in which the “center” of scattering is anticipated to have occurred. In accordance with the central limit theorem for sampling, the confidence interval constructed from the mean statistic of the approximately Gaussian-distributed scattering angles converges upon the actual z-value parameter being sought. The accumulation of data points will occur until the p-value derived from the test statistic in a 1-sample t-test.

2.3.4 Increase of photon detection efficiency (PDE)

After finding that the optical yield from mean muon momenta through a scaled up model of the device would be insufficient when deriving differential signals between pixels (approximately 24 microcell firing events were projected to occur near the minimally ionizing point in polyvinyl toluene of the muon energy spectra, specifically 325 MeV)⁶, the decision was made to examine a parabolic optical cavity system using dielectric coating and lenses to conserve light output and to reproject the image of the muon ionization onto the surface of a solid state SiPM array.

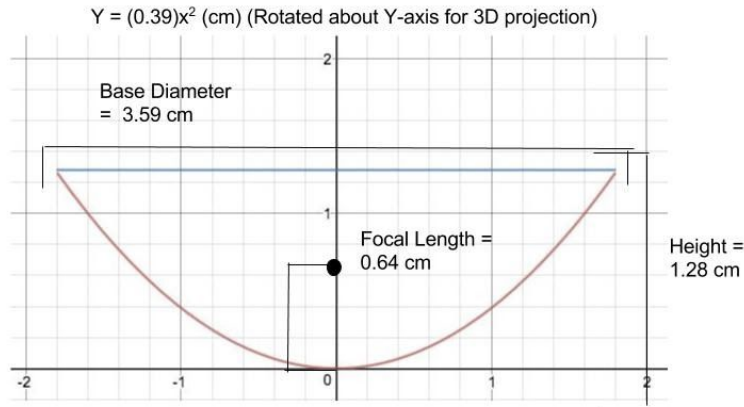


Figure 2.3.4.1

The concept of using a parabolic mirror was examined to improve the intensity of light given off by the scintillators. This would allow for a better differentiation between SiPM signals from noise and real muon instances. Implementing this concept on an actual device would require the use of a Bragg mirror (dielectric coating) along the outside of a parabolic scintillator to reflect the light back towards the SiPM array which would be placed near the focus of the parabola. The dielectric coating gets continuously more reflective when more layers of the coating are applied. Weighing both cost and reflectiveness of the dielectric coating, it was determined that there would be four total layers of the dielectric coating. With four layers, 83.4% of the light given off from the scintillator would be received by the SiPM compared to 0.54% of the light which would have been received without incorporating a parabolic mirror. This mirror would reflect back 90.6% of the light given off from the scintillator; there would be a slight loss in light due to its attenuation through the scintillator.

The percentage of light reflection from the surface of a dielectric coating can be ascertained by

$$R(\%) = \left(\frac{1-n_e}{1+n_e} \right)^2$$

where n_e is the composite index of refraction given by

$$n_e = \frac{(n_h)^{2p+2}}{(n_s n_L)^{2p}}$$

In the above expression, n_s is the index of refraction of the substrate onto which the dielectric coating is deposited, in this instance, the polyvinyl toluene scintillator material. n_h and n_L respectively correspond to the alternating indices of refraction from the “lower” and “higher” constituents of the coating.³² p is an integer referring to the number of pairs of the dielectric layers that are incorporated into the coating. For this application, titanium dioxide (TiO_2) and magnesium fluoride (MgF_2) are the selected materials for the coating, because their relative indices of refraction in thin-film applications are optimal for reflecting in the wavelength emission range of the PVT scintillator. For dielectric high reflectors, the steep boundaries of wavelength reflection versus transmittance is determined by

$$\lambda_{edge} = \frac{\lambda_0}{1 \pm \Delta},$$

where λ_0 is the targeted peak reflectance wavelength and Δ is given by

$$\Delta = \frac{1}{90} \arcsin\left(\frac{n_h - n_L}{n_h + n_L}\right)$$

Below is the listed indices of refraction for titanium dioxide, magnesium fluoride, and the polyvinyl toluene substrate. With the intention to at least reach a 90 percent rate of photon reflection, four (P) alternating depositions of the two aforementioned thin film materials are required for the Bragg reflector cladding on the scintillating modules.

Dielectric coating specification	Value
TiO ₂ : n _h (index of refraction)	2.4
MgF ₂ : n _L (index of refraction)	1.19
PVT: n _s (index of refraction)	1.58
P (number of alternating layers)	4
R(%) (reflectance ratio)	90.6%

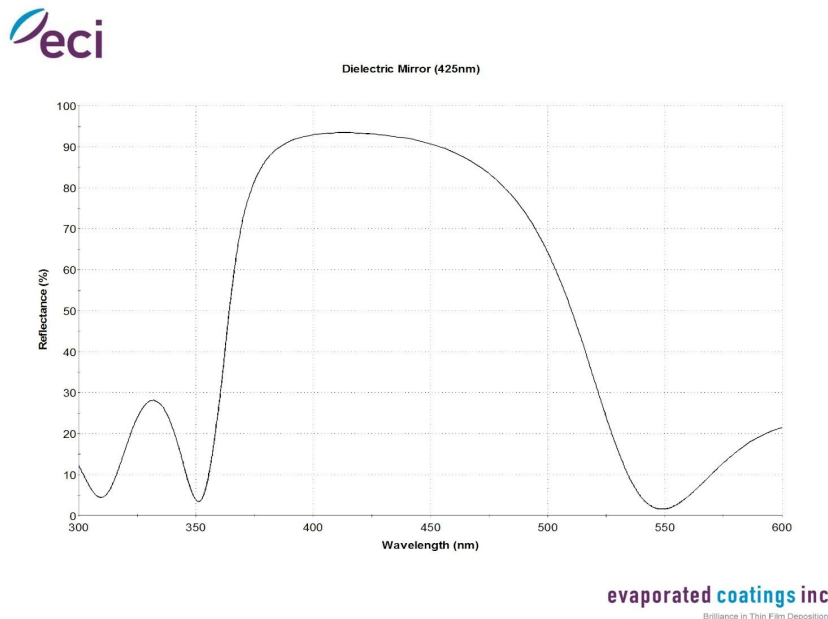


Figure 2.3.4.2

Figure 2.3.4.2 shows the proportional reflectance of the proposed dielectric cladding specifications given the incident wavelength of light. The peak reflectance is optimized to be situated in proximity to the peak wavelength of scintillator emission, while still making use of titanium dioxide and magnesium fluoride, both

of which are relatively inexpensive compounds to incorporate into the manufacture of Bragg reflector systems.

The implementation of a lens over each individual photomultiplier allows for an increase in photon detection efficiency due more light being captured and redirected toward respective SiPM pixels. Despite the lens absorbing some of the light that attempts to pass through it, there will still be a net gain in PDE when using lenses to focus the light towards the SiPMs.

2.3.5 Scaled up rendition

The scaled up version accounts for real world implementations and includes both aspects introduced in [2.3.4]. Four separated SiPM's spread across the flat horizontal scintillator surface are implemented instead of 2x2 arrays to allow for a larger detection area per SiPM. The sensing systems are surrounded hexagon shells which are intermeshable and easy to orientate into a honeycomb structure. This allows the device to be customizable in size depending on how many systems a client can acquire. This feature gives the device the potential to considerably increase muon flux and reduce scan time (see [5.2]). One sensing block including the photomultipliers, a parabolic scintillator, and hexagonal shell is depicted in figure below.

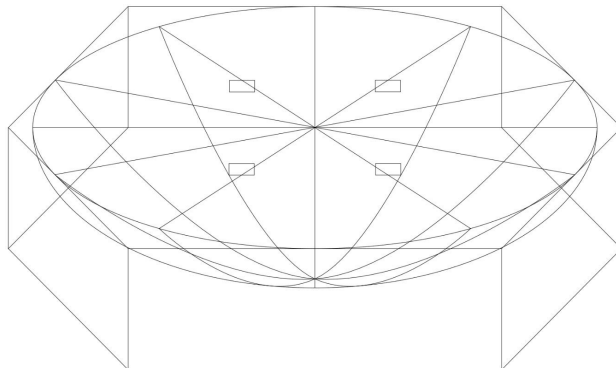


Figure 2.3.5.1

3 Materials and Methods

3.1 Polyvinyl toluene based scintillator

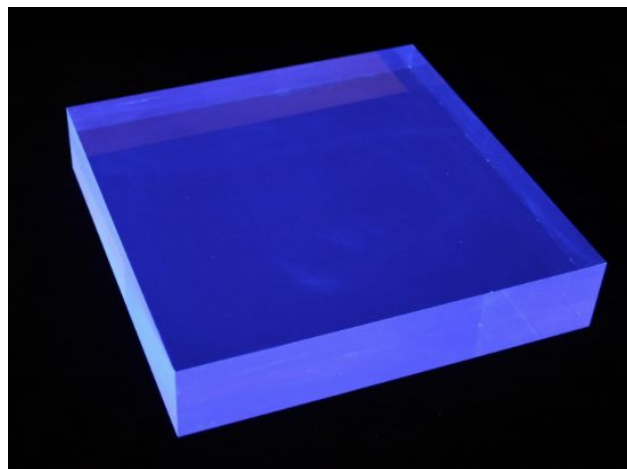


Figure 3.1.1²

Scintillating materials re-emit deposited energy from incident forms of ionizing radiation at an energy transfer efficiency on the order of 3 percent as optical photons.⁴ Massive, charged particles lose energy by interacting with atomic electrons and are detected as a result via elastic collisions. Soft collisions result in valence orbital excitations, causing the material to exhibit small-magnitude fluorescence. Hard collisions involve transfers of sufficient energy between the incident form of ionizing radiation that produces a large-magnitude scintillation response. Secondary ionization may result from scintillated photons that dislodge valence electrons, which in turn deposit their kinetic energy into the scintillator substrate. Organic scintillators consist of a plastic polymer substrate doped with primary and secondary fluor compounds. Following the ionization of the plastic base, energy is transferred on the order of 10 nm to a primary fluor molecule, which in total composes ~1 percent of the weight of the scintillator. From the primary fluor, a UV photon ($\lambda \approx 340$ nm) traverses a distance on the order of 100 μm , terminally activating a secondary fluor molecule (wavelength shifter) that re-emits optical photons in a target wavelength interval.

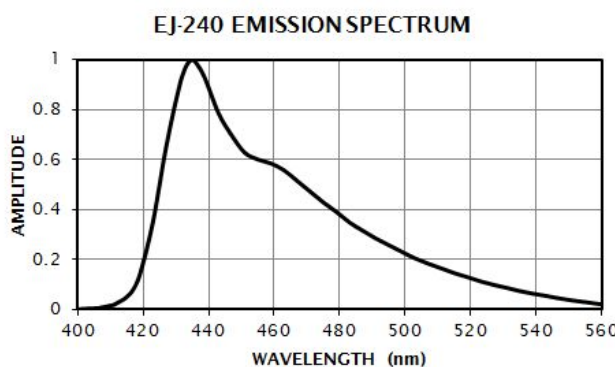


Figure 3.1.2

PROPERTIES	
Light Output (% Anthracene)	41
Scintillation Efficiency (photons/1 MeV e)	6,300
Wavelength of Maximum Emission (nm)	430
Light Attenuation Length (cm)	240
Decay Time (ns)	285
H Atoms per cm^3 ($\times 10^{22}$)	5.19
C Atoms per cm^3 ($\times 10^{22}$)	4.68
Electrons per cm^3 ($\times 10^{19}$)	3.33
Density (g/cm 3)	1.023

Polymer Base	Polyvinyltoluene
Refractive Index	1.58
Softening Point	75°C
Vapor Pressure	Vacuum-compatible
Coefficient of Linear Expansion	7.8×10^{-5} below 67°C
Temperature Range	-20°C to 60°C
Light Output (L.O.) vs. Temperature	At 60°C, L.O. = 95% of that at 20°C No change from -60°C to 20°C

Figure 3.1.3²

The organic polyvinyl toluene scintillator, EJ-240 from Eljen Technologies, was selected for its peak emission wavelength of 430 nm in order to maximize the photon detection efficiency exhibited by the SiPMs with a peak detection wavelength of 420 nm. Additionally, the long decay time of EJ-240 (285 ns) reduces the time constraint put on the analog to digital conversion due to the transience of single muon ionization events. The scintillators possessed volumetric geometries that are intended to maximize the volume to surface area ratio while maintaining a relatively small cross-sectional profile. This geometry minimizes the loss occurred by the inverse square expansion of the light sphere from individual ionization events while maximizing the total frequency of muonic-electron interactions over the course of its trajectory through the scintillator cube. The maximization of muonic-electron interactions ensures that a sufficient light yield is emitted for a differential optical flux to be measured on the SiPM diamond-milled face of the scintillator. The light attenuation length of EJ-240 indicates the distance over which a collimated beam of EM radiation will be reduced in its intensity by a factor of e-1 ($\sim 74\%$). This light attenuation length of 240 cm is 94 times the diameter of the 2.54 cm^3 scintillator cubes employed in the prototype. This reduces the degree of scattering shown in the relative optical flux distribution on the SiPM face caused by secondary fluorescence that occurs when a photon undergoes a photo-electric energy transfer with a valence electron.

3.2 Silicon photomultiplier array

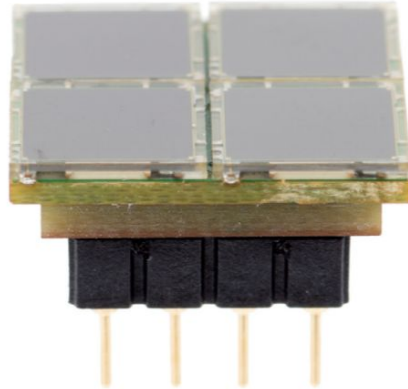
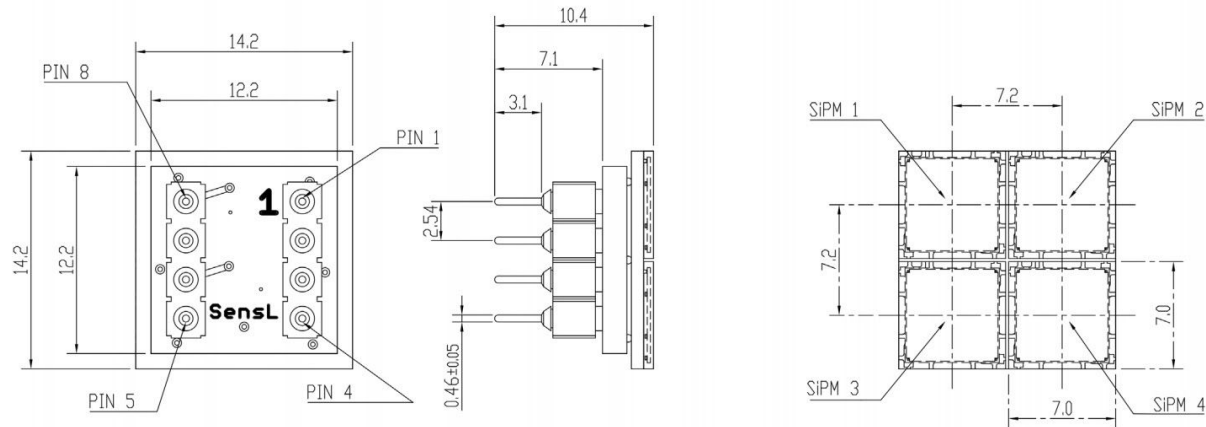


Figure 3.2.1'

Detection of single-photon instances are fortunately made possible by photomultiplier tubes and Geiger-mode avalanche photodiodes. Photomultiplier tubes consist of a scintillating material and various dynode layers within a vacuumed, glass tube which enhance and multiply photon incident signals. In engineering the prototype, the decision was made to opt for solid state SiPM arrays instead of the commonly-used photomultiplier tubes for various reasons.

Figure 3.2.2^l

Board (area)	14.2 mm ²
Peak wavelength (λ_Q)	420 nm
Total number of microcells (pixel)	18,980
Microcell fill factor	64%
Capacitance (pixel)	3400 pF
Breakdown voltage	24.5V (2.5V overvoltage)
Microcell recharge time constant	95 ns
Dark count	Typically 1200 kHz (maximum of 3400 kHz)
Crosstalk (probability)	7%
Afterpulsing	0.2%

Each of the four silicon photomultiplier pixels is composed of a single CMOS microcell array consisting of 18,980 microcells (an avalanche photodiode in Geiger-mode and a quench resistor). When a photon is incident upon one of these avalanche photodiodes, there is a rapid discharge current that decays exponentially when the voltage spike is dissipated across the quench resistor. A scaling output forms when the currents of all of these microcells are summed to show the approximate number of microcells discharging at a given time, which is indicative of the intensity of incident light, based on the particular quoted gain for the photomultiplier. The minimally ionizing muon energy level for PVT scintillation (325 MeV) will activate approximately 24 microcells (as stated in [2.3.4]) (assuming that the hypocenter of photon emission is the center of the cubic scintillator), thus releasing a peak current of 63 μ A. The microcell activation count is dependent on the photon detection efficiency of the SiPM and the attenuation/dispersion effects on the light stream prior to its encounter with the surface of the SiPM (see

$N_{microcells}$ in [3.5.2]). The average current was determined by using the quoted photoelectric gain of the microcells in the SiPMs and the decay time constant. A 75th percentile (using the Gaisser equation in [3.5.1]) muon energy level allow the SiPM array to output 715 mA.

3.3 Shielding

Lower energy particles must be filtered out to prevent non-muonic ionization instances from occurring. Low energy particles will decay and become insignificant through a steel shielding while the higher energy particles lose a massive amount of energy, converging to a mean of 800 MeV to 10 GeV.



Figure 3.3.1

An open, rectangular prism of 16 gauge weldable steel was sheared, welded together, and placed around the prototype as seen in the figure above. In the scaled up rendition, shielding placement would follow traditional requirements presented in the drift chamber implementations of muon scattering tomography, where a large steel exoskeleton encases the unified structure.

3.4 Electronics

3.4.1 Procedure

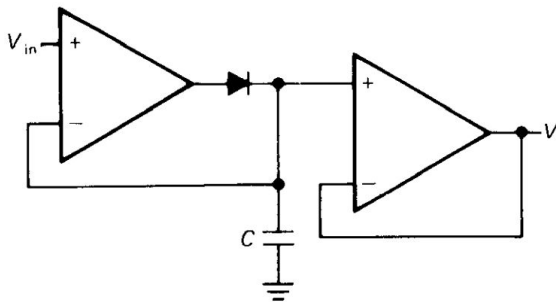
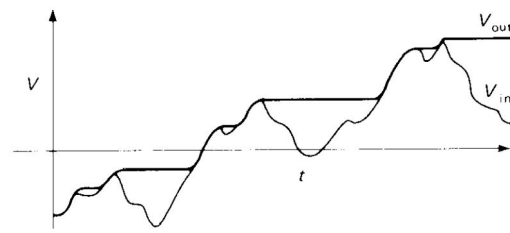
Preparation for electrical signal processing requires fixed set of specifications. The SiPM arrays and multiple IC's in the readout circuitry call for regulated current in order to function. An HP Power Supply (6215A) was used to power the entirety of the prototype, which include the sensory SiPM's, operational amplifiers, and a data acquisition module. Calibration of readout circuitry calls for a simulated, electrical muon incidence, which is done by a signal generator (Wavetek 10 Mhz DDS Function Generator (model 29)). For calibration purposes and lack of analog-to-digital converters, oscilloscopes (manufactured by Tektronix) are used to visualize electrical current throughout various stages of circuitry.

3.4.2 Signal processing

The output each individual quadrant of the SiPM arrays consists of a steady voltage near ground with a fluctuation in voltage due to noise. The lowest energy muon will produce a signal of $63 \mu\text{A}$ (as stated in [2.3.4]), which is 20mV when flowing through the SiPM circuitry. Another constant to take into consideration is the microcell recharge rate (see [3.2]). Twice that constant is an approximate length of a signal put out by each SiPM, equalling 5.26 MHz . Readout circuitry was designed around this calculated value to insure the lowest energy muon expected will still be detected. There are a total of four stages in processing the signal to enter AD conversion: crude signal preparation (AC separation, voltage buffer, and re-addition of static DC), signal amplification, peak detection, and timing.

The first stage of crude signal preparation utilizes a coupling capacitor to block excess DC voltage and noise from being processed. A voltage follower is used as a buffer to match impedance levels of the SiPM circuitry (high output impedance) and the readout circuitry (low input impedance). Alas, a regulated amount of DC is added back to the signal, carrying it away from ground; the following op amp (AD8055A) is unable to amplify a signal near ground. The second stage entails an amplifying op amp which has gain of 35 dB (55 times amplification at 5.26 MHz), allowing the lowest 20mV signal to create a disparity of 1V in output voltage.

The third stage utilizes a simple “sample and hold”-type circuit (figure 3.4.2.1) which is used to detect the peak (figure 3.4.2.2). The first AD8055A op amp charges up the capacitor which will continue to hold the voltage steady at its highest peak until it is drained. A BJT is situated before the capacitor, allowing it to be discharged when receiving a digital command. The peak is extended so that slower ADC's and data acquisition microcontrollers are allowed to fully interpret and analyse the incoming data.

Figure 3.4.2.1³Figure 3.4.2.2³

Though the signal is already processed, a Schmitt trigger is used for timing in the fourth stage. A timing system is imperative to the successful implementation of the trilateration algorithm, as it both enables the linkage of disparate scintillation events between scintillators during the reconstruction phase of data acquisition. The purpose of the Schmitt trigger is to detect the immediate edge of a signal, producing a large negative voltage from the moment of increase of the signal. When each pixel of the total sixteen have a Schmitt trigger, timing is between each sensing module is determined.

3.5 Monte Carlo procedure

The goals of the Monte Carlo simulation were to generate sample tomographic output graphics for both prototype and scaled-model design, quantitatively compare efficacy of prototype and scaled parabolic optical cavity model designs by metrics of temporal efficiency, cost efficiency, and maximum voxel resolution, and quantitatively compare metrics of scaled parabolic optical cavity model to drift chamber apparatus.

The trilateration algorithm and scan volume reconstruction in the simulation incorporated Schmitt trigger based timing data and differential current discharge from pixels within four photomultiplier arrays to emulate data acquisition system. Time efficiency was modeled by randomly generating data compilation events from incident muons that underwent Gaussian angles of scattering. This enabled a scalable threshold of muon incidences to be required for each volumetric pixel (voxel) in order to achieve the benchmark of 95% certainty in the standard deviation of multiple-Coulomb scattering in at least 95% of voxels, or that corresponding to other p-values.

The primary difference between the prototype and scaled models corresponds to the photon behavior interior to the scintillator as well as the dielectric medium boundary. The algorithm for simulating the scaled up model summates total photon retention by estimating maximum pathlength through truncated paraboloid volume, and applying the coefficient of attenuation as well as singular dielectric medium interaction loss to the total photon emission. The number of parabolic optical cavities (arranged in honeycomb structure) was adjusted for different trials.

3.5.1 Muon source generation

The efficacy of the muon scattering tomography prototype was assessed through a six-stage stochastic simulation consisting of muon generation, propagation, muon-scintillator interaction, photon-SiPM interaction, electronic signal generation, and scan volume reconstruction. The core of the simulation was written in Java and visualized with MATLAB. Randomized muon generation was conducted with the Gaisser function

$$\frac{dI_\mu}{dE_\mu} \approx 0.14 \left(\frac{E_\mu}{GeV} \right)^{-2.7} \left[\frac{1}{1 + \frac{1.1E_\mu \cos\theta}{115 GeV}} + \frac{0.054}{1 + \frac{1.1E_\mu \cos\theta}{850 GeV}} \right]$$

describing the differential flux in respect to the zenith angle of the incident muon. This equation was used to generate randomized muon events in conjunction with the proportion of the muon angular flux to the function $\cos^2(\theta)$. The energy spectra was modeled as being approximately Gaussian with a mean of 4 GeV. A “MuonController” class logged the positional vectors of all generated muons within the system and updated their momenta and kinetic energies at each cycle of the simulation. The timescale of the simulation was adjustable, however all tests were run at a 1 ns time interval between discrete cycles. At the progression of each cycle, “Muon” objects were advanced along their inbound trajectories and their zenith and azimuthal angles continuously modified to account for the probability of minute Coulombic scattering events. Positional, velocity, and momentum-energy vector systems were used to bridge periodic multiple-Coulombic scattering events with alteration to muon propagation. The Lorentz transform was implemented for momentum four-vectors. Continual energy losses were used as feedback for time dilation coefficient to adjust for this effect when determining location of muon decay or absorption into muonic atom. Relativistic mass,

$$m = \frac{m_0}{\sqrt{1 - \frac{v^2}{c^2}}},$$

relativistic energy,

$$KE = mc^2 - m_0c^2,$$

and time dilation

$$T = \frac{T_0}{\sqrt{1 - \frac{v^2}{c^2}}} = T_0\gamma$$

were used to describe various relativistic effects on the muon that were accounted for in throughout experimentation and simulation design.

3.5.2 Muon propagation

At each scattering event, the energy deposition or inelastic loss was approximated according to the Bethe-Bloch function,

$$-\langle \frac{dE}{dx} \rangle = \frac{4\pi}{m_e c^2} \cdot \frac{n_e^2}{\beta^2} \cdot \left(\frac{e^2}{4\pi\epsilon_0} \right)^2 \cdot \left[\ln\left(\frac{2mc^2\beta^2}{I(1-\beta^2)}\right) - \beta^2 \right]$$

which is optimal in use for measuring bulk dosages of energy deposition per distance through a material cross-section due to its empirical inclusion of skew from disproportionately high levels of ionization energy transfer by muons in the Bethe-Bloch region of the momenta-energy deposition plot. The time dilation coefficient was assessed at each cycle subsequent to kinetic energy and velocity adjustments in order to tabulate a total duration of time experienced by the muon in transit, such that substantial energy losses would result in the expedited decay of the muon prior to entering the lithosphere.

After muon passage through the shielding structure, it is predicted that the muon energy spectra will significantly converge towards the minimally ionizing region of the momentum-energy deposition plot thus meriting the usage of the Landau distribution

$$\Delta p = \xi \left[\ln\left(\frac{2mc^2\beta^2\gamma^2}{I}\right) + \ln\left(\frac{\xi}{I}\right) + 0.2 - \beta^2 - \delta(\beta\gamma) \right]$$

$$\xi = \left(\frac{K}{2}\right) \langle \frac{Z}{A} \rangle \left(\frac{x}{\beta^2}\right)$$

as a template for determining the rate of energy loss exhibited by a muon incident through the prismatic scintillator. The function given by Birks' law

$$dL = S \cdot \frac{dE}{1+k_B \frac{dE}{dx}}$$

was used to describe light emission as a function of energy deposition. The scintillation efficiency S , is a ratio of emitted photons to energy deposited in a scintillator.

Similar to the shielding and air material cross-section propagation segments, the modelling of the muon propagation through the polyvinyl toluene scintillator included multiple-Coulomb scattering projected over a continuous interval and with consistent energy losses inversely proportional to the radiation attenuation length. At each timestep for muons undergoing passage through a scintillator, a localized “photosphere” was produced, comprised of a nite array of “Photon” objects with trajectory and wavelength attributes. Each “Photon” object endures the application of a filter each timestep to represent the effects of light attenuation interior to the scintillator. The outward spread of the photosphere from the original site of ionization adheres to the inverse square relation for the optical intensity per steradian and the outward radius travelled. This enabled the logging of photon passage counts for each quadrant on the scintillator face where the SiPM is intended to be mounted, which after being funnelled through the grid interpolation function in MATLAB could be visualized as a plot demonstrating the differential optical flux on the y-z

plane. The differential optical flux was converted to a high-resolution distribution of incident photons on the y-z plane via a Riemann sum process. These photons were subsequently injected into “SiPM” objects, each of which possessed a 2-D array of “Microcell” objects, in order to stochastically activate microcell Geiger discharge events.

3.5.3 Photomultiplier output model

Current discharge was modeled according to an equivalent circuit scheme, where the Geiger-mode photodiode is treated as a voltage source in the readout system. The decay time, rise time, photodiode capacitance, quench resistance, quench capacitance, and parasitic capacitance of the system were taken into account, modeled after the specifications issued by the SensL company for the MicroC-6 mm SiPM. Thermal noise was modelled according to a Poisson distribution, with optical crosstalk and afterpulse microcell states included. Independent tests of the SiPM behavior were conducted with virtual photon injection per nanosecond to compare muonic signal output to thermal noise background. Two-sample t-Tests were implemented to assess whether the minimally ionizing muon energy would yield a current peak that is significantly removed from background noise from the perspective of a 40 MHz ADC module (the results are used to justify the adoption of a peak detection circuit for readout versus a standard raw ADC signal treatment, see section 4.2.2.2). The three-dimensional scan volume was constructed over a specified duration by allocating scatter events to their respective voxels and by accumulating a confidence interval for the parameter σ_0 which represents the standard deviation of all muon scattering exhibited for a voxel z-value. The power P of each muon scatter datapoint was also scaled with increased muon momentum, because of the reduced probability for significant scattering to occur in the atmosphere or scintillating cross-sections.

The SiPM behavior was modelled using an empirical formulation of photodiode output current as a function of time since an initial photoelectron induced avalanche. The model shown below is the result of the work contained in *Simulating Silicon Photomultiplier Response to Scintillation Light*.²⁵ Input values include diode resistance, quench resistance, parasitic capacitance, quench capacitance, diode capacitance, and the gain exhibited by an individual microcell embedded in the SiPM. The figure below shows the equivalent circuit model that the microcell current output model is based on. From the left, a voltage bias is applied such that there exists a calculable potential difference across the reversed photodiode (V_d in excess of the breakdown voltage), the quench resistor (V_q), and the remainder of the microcell array (to form the storage of charge in the parasitic capacitance - V_1 - and the voltage across all other microcell diode and quench resistance components - V_2). The chart below contains the variable specifications for the model (values contained within the subsequent UML diagram:

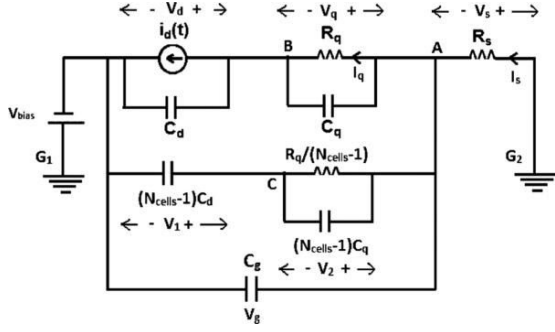


Figure 3.5.3.1²⁵

$$I_s(t) = G e \left[a_1 \exp\left(\frac{-t}{\tau_{cd1}}\right) + a_2 \exp\left(\frac{-t}{\tau_{cd2}}\right) + a_3 \exp\left(\frac{-t}{\tau_{md}}\right) + a_4 \exp\left(\frac{-t}{\tau_{mr}}\right) \right]$$

$$\tau_{\text{md}} = C_d \frac{R_d R_q}{R_d + R_q}$$

$$\tau_1 = R_q (C_q + C_d)$$

$$\tau_2 = R_q C_q$$

$$\tau_3 = R_s N_{\text{cells}} C_d$$

$$\tau_4 = R_s C_{\text{go}}$$

$$\tau_{cd\,1}, \tau_{cd\,2} = \frac{\tau_1 + \tau_3 + \tau_4}{2} \pm \frac{\sqrt{(\tau_1 + \tau_3 + \tau_4)^2 - 4(\tau_1\tau_4 + \tau_2\tau_3)}}{2}$$

$$a_1 = \frac{\tau_{\text{cd}1} (\tau_{\text{cd}1} - \tau_2)}{(\tau_{\text{cd}1} - \tau_{\text{cd}2})(\tau_{\text{cd}1} - \tau_{\text{md}})(\tau_{\text{cd}1} - \tau_{\text{mr}})}$$

$$a_2 = \frac{\tau_{\text{cd}2} (\tau_{\text{cd}2} - \tau_2)}{(\tau_{\text{cd}2} - \tau_{\text{cd}1})(\tau_{\text{cd}2} - \tau_{\text{md}})(\tau_{\text{cd}2} - \tau_{\text{mr}})}$$

$$a_3 = \frac{\tau_{\text{md}} (\tau_{\text{md}} - \tau_2)}{(\tau_{\text{md}} - \tau_{\text{cd}1})(\tau_{\text{md}} - \tau_{\text{cd}2})(\tau_{\text{md}} - \tau_{\text{mr}})}$$

$$a_4 = \frac{\tau_{\text{mr}} (\tau_{\text{mr}} - \tau_2)}{(\tau_{\text{mr}} - \tau_{\text{cd}1})(\tau_{\text{mr}} - \tau_{\text{md}})(\tau_{\text{mr}} - \tau_{\text{cd}2})}$$

$$N_{\text{fired}}(M, V, \lambda) = M \left(1 - \exp \left(- \frac{PDE(V, \lambda) \cdot N_{\text{ph}}}{M} \right) \right)$$

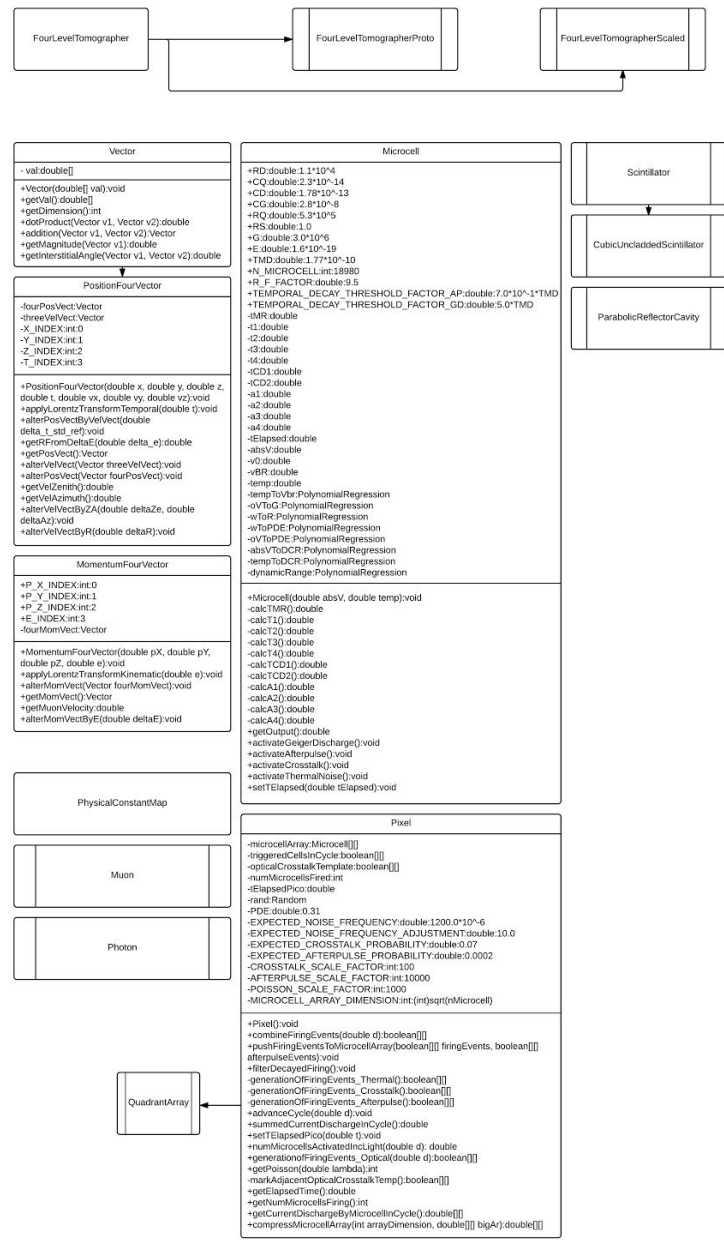


Figure 3.5.3.2

4 Results

4.1 Calibration

Calibration and assessment of the device performance was segmented into three stages: first the analog signal amplitude and rise/fall times was analyzed in order to determine optimal values for bit resolution, gain requirement of op-amp setup for signal amplification trigger threshold for sample-and-hold circuit, as well as the delay parameter for the BJT controlling the release of the peak detection phase (see [3.4.2]). Analog signals were derived from a UV LED beam (through a 1.8 mm diameter aperture), in order to observe fluctuation in the analog signal from modulating total energy deposited in the scintillator, and the differential signal generated in each SiPM as the beam coordinates, pitch, and yaw were manipulated.

This data was compiled to develop an algorithm for beam trilateration and calculation of trajectory. A dark count (see [3.2]) test was conducted to evaluate microcell Geiger activation rates by thermally-induced noise, such that an empirical distribution of this effect could be constructed to compare to signal output, in order to conclude significance thresholds for muon point detection (figure 4.1.2, bottom left).

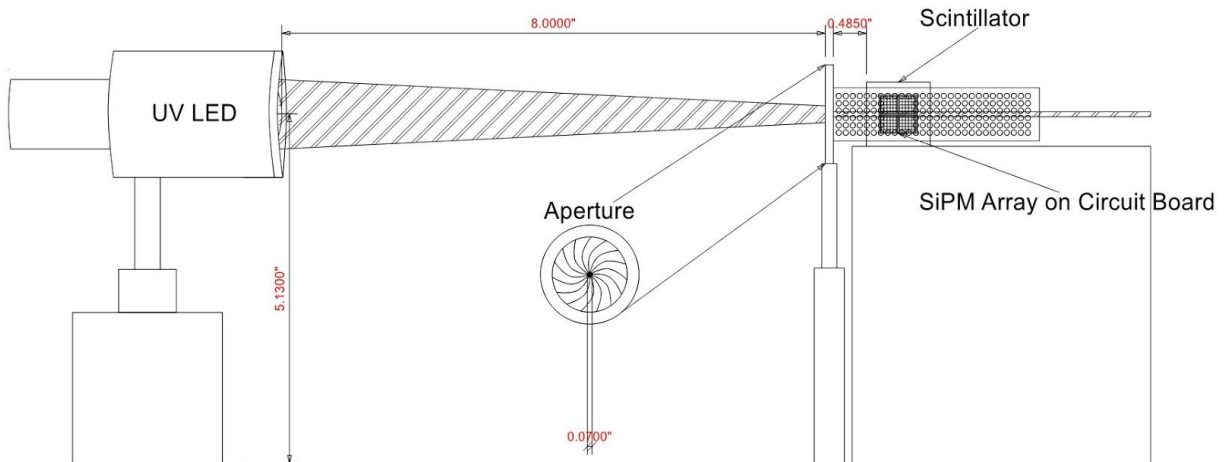


Figure 4.1.1

The signal output was measured with a high frequency oscilloscope (Tektronix 200 MHz Oscilloscope Digital Storage (2024C)), so that necessary information to fully design readout circuitry for single-count muon detection is acquired. Channel 1 (orange) represents pixel 1 (see [3.2]) and channel 2 (blue) represents pixel 4 [3.2] for all figures below.

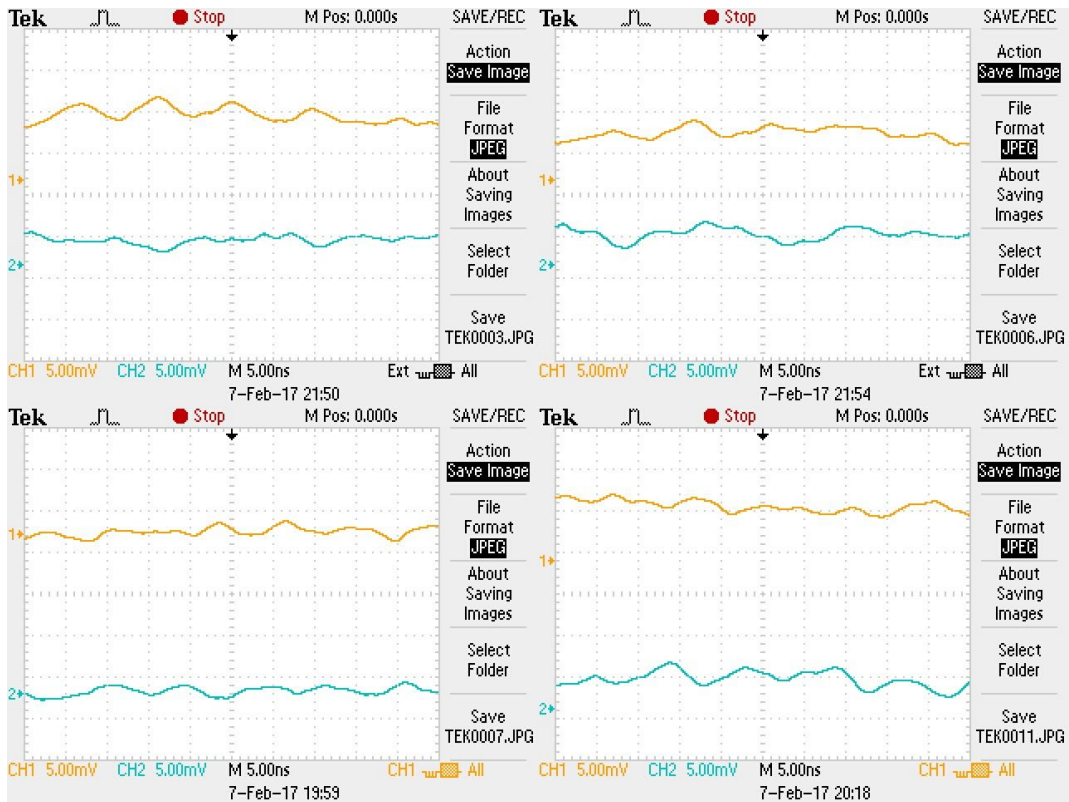


Figure 4.1.2

The top 2 oscilloscope readouts in figure 4.1.2 depict calibration testing for the trilateration algorithm. The closer the LED was to the corresponding pixel, a higher voltage signal was supplied to the oscilloscope. This proves the hypothesis on the use trilateration in muon detection since the difference in signals from the pixels based on the lights impact point on the scintillator is able to be discerned. This lower-energy simulation is more characteristic of a muonic signal because the photomultipliers are removed from their nonlinear saturation interval. It was also consistently observed a higher voltage supplied by pixel 1 due to the UV LED scattering directly when entering the scintillator, emitting less intense quantities to pixel 4.

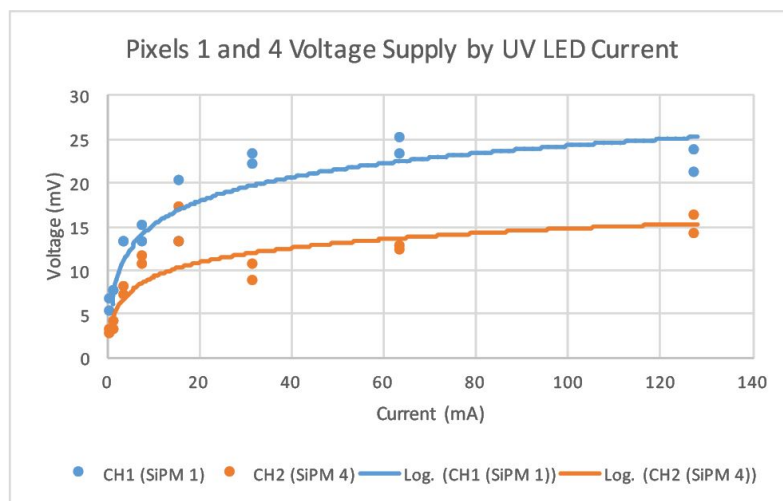


Figure 4.1.3

Logarithmic scaling of current driven through the UV LED enabled the observation of the SiPM output reaching nonlinear saturation (as seen in figure 4.1.3), which occurs because of the increasing ratio between incident photons at peak detection wavelength and the discrete microcell count.

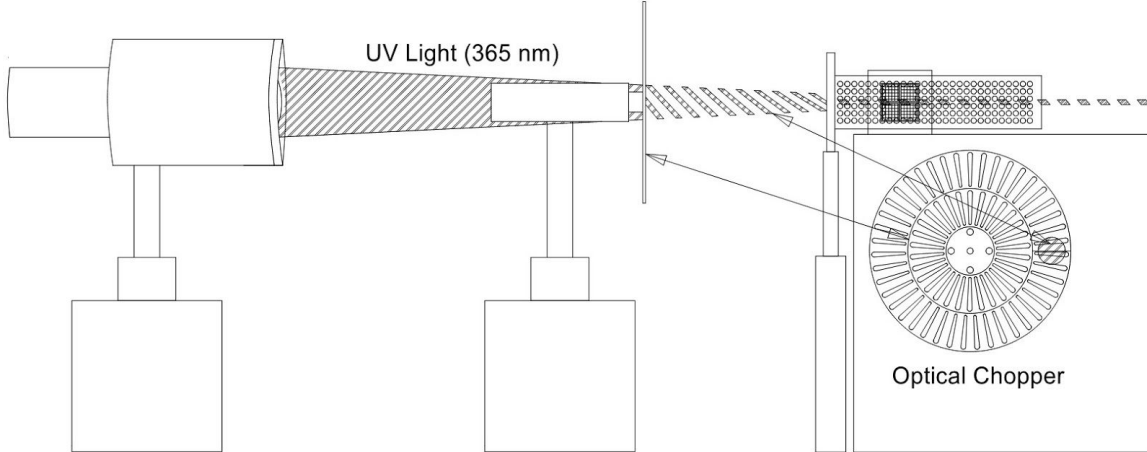


Figure 4.1.4

The optical chopper in figure 4.1.4 was employed to model the SiPM output when two different microcell ring equilibria were alternated in a short timer interval. The pulse shape was observed and recorded over the duration of the signal derived from the UV LED segmented by an optical chopper. In the various oscilloscope readouts presented, four separate chopper speeds are used in figure 4.1.5.

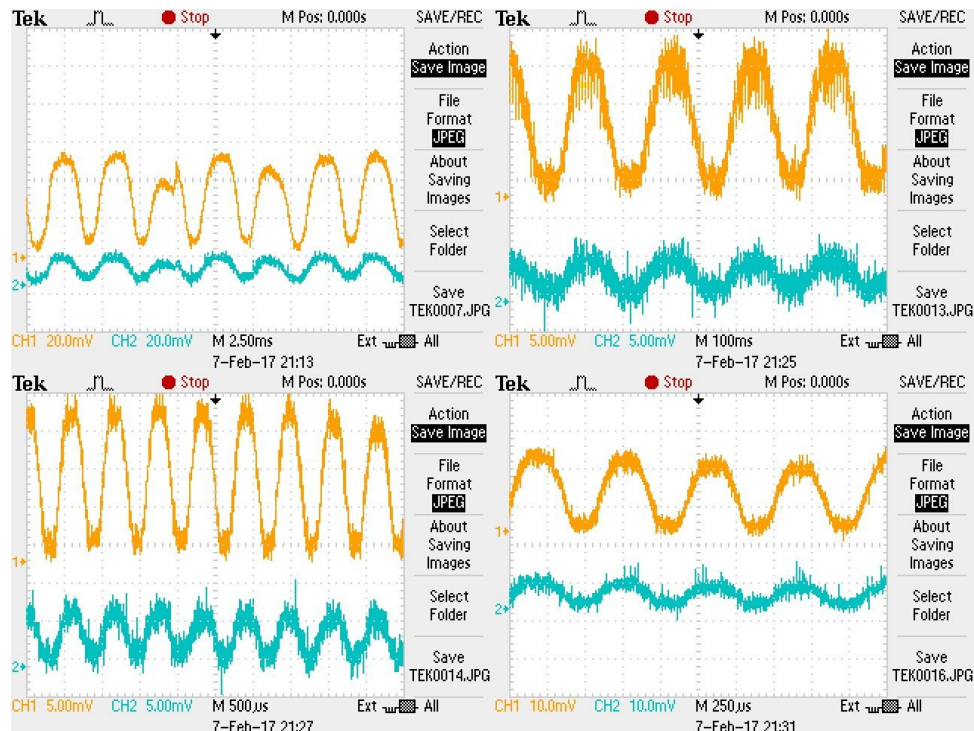


Figure 4.1.5

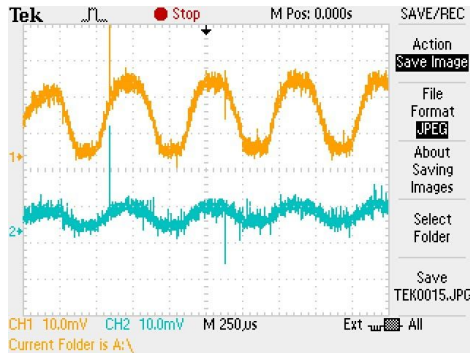


Figure 4.1.6

In this readout with oscilloscope time interval of 250 μ s, similar to bottom right graph on figure 4.1.5, we are able to see fluctuations in thermal and electrical noise from the two SiPM's. There is also an unexpected high energy particle instance at the beginning of the graph, fitting the general requirements on expected signal period and amplitude.

4.2 Simulation

4.2.1 Electrical simulation

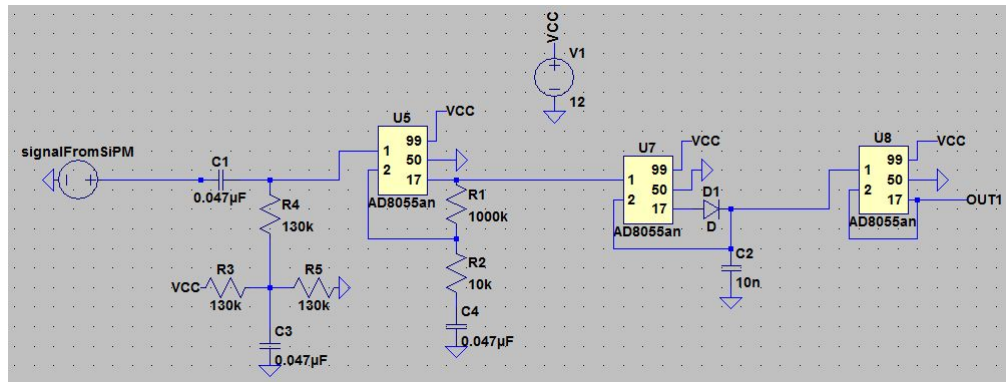


Figure 4.2.1.1

The simulation of electronics was developed using LTSpice. Spice files of integrated circuits were provided by manufacturers and distributors of the product, resulting in accurate simulation results. Refer to [3.4.2] for stage descriptions.

First stage is visualized by the system (one coupling capacitor and various resistors with capacitor for op amp biasing) after the voltage supply “signalFromSiPM” and before “U5” in figure 4.2.1.1. Stage 2 in figure 4.2.1.1 is portrayed by non-inverting AD8055A op amp “U5” with required determinants of gain below (2 resistors for voltage dividing and a capacitor to ground). Stage 3 is depicted in figure 4.2.1.1 by the two AD8055A op amps to allow for peak detection. Schmitt trigger of stage 4 is not shown while it is not necessary for the signal processing simulation.

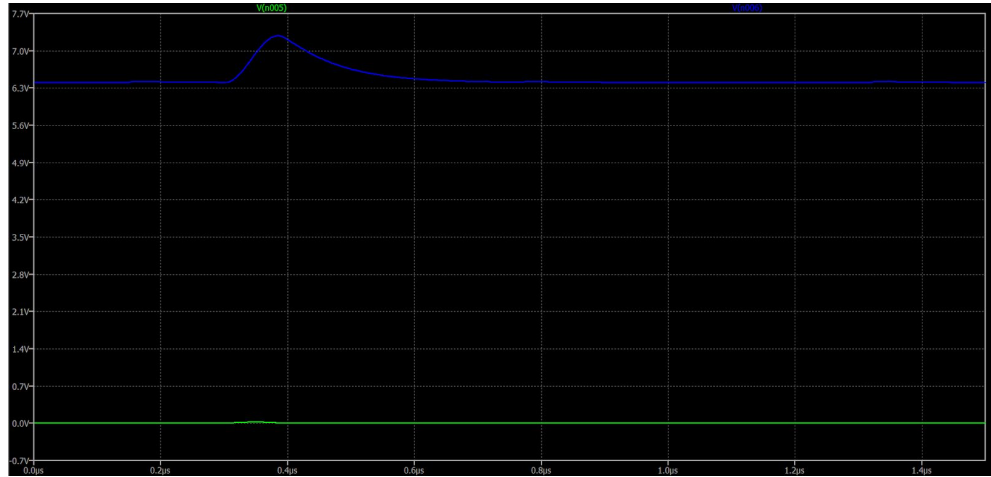


Figure 4.2.1.2. Green line represents raw signal immediately after the first coupling capacitor in stage 1. Blue line represents the resulting signal after passing through the entirety of stage 2.

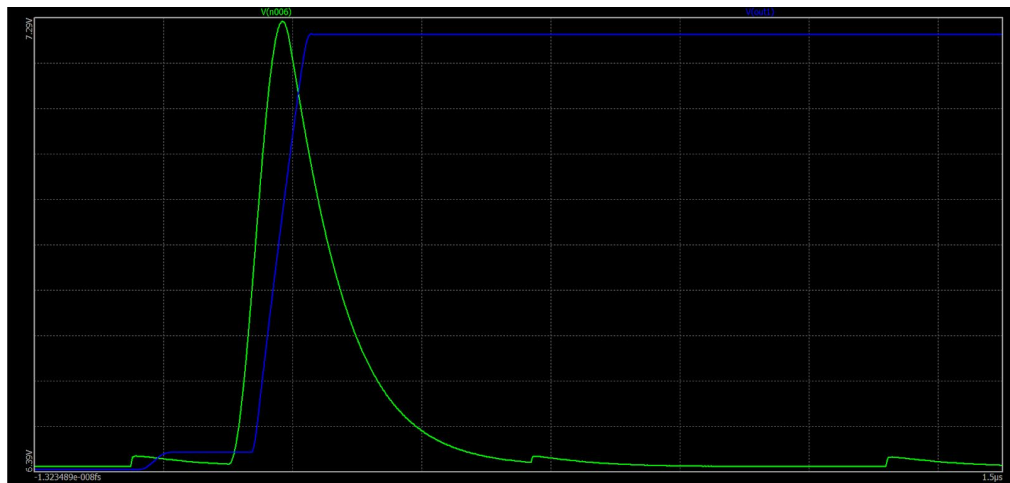


Figure 4.2.1.3. The blue line in figure 4.2.1.2 is reconstructed at a different visual scale as this green line. Blue line here represents the result of stage 3, peak detection.

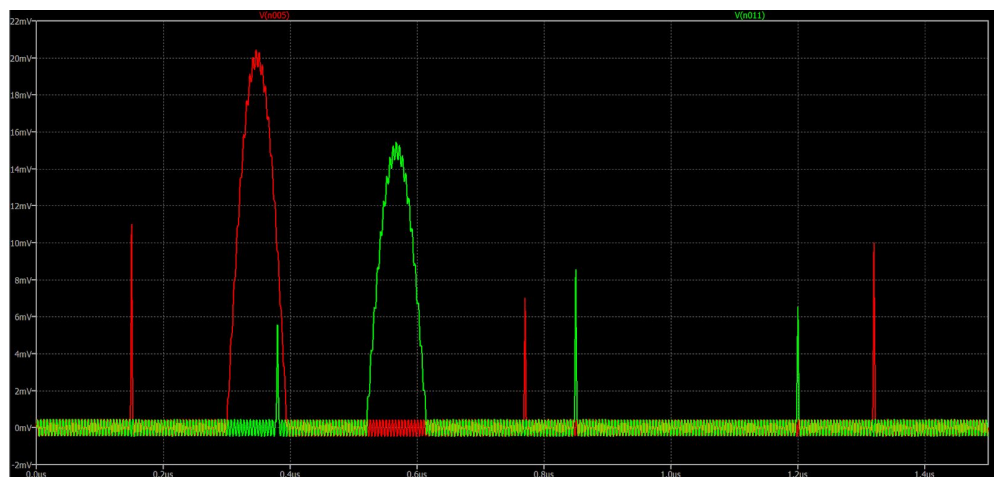


Figure 4.2.1.4. Two muon instances (thermal noise, microcell crosstalk, and other varieties of noise are taken into account) are simulated.



Figure 4.2.1.5. Same red and green lines as figure 4.2.1.4 show the final, processed signal which are immediately fed into ADC's. The original disparity of 5 mV now has a ~ 0.1 V difference, allowing values to be easily read.

4.2.2 Monte Carlo simulation

4.2.2.1 Temporal efficiency

The Monte Carlo simulation procedure was adapted to produce estimates of temporal efficiency by running long-term accumulation cycles of muon data until the probabilistic threshold (set to 95 percent for both the confidence level in multiple-Coulomb scattering parameter estimation and the total proportion of voxels with that level) and to output the associated scan durations for that extent of data accumulation.

4.2.2.2 PDE

Three simulative scenarios are depicted in the series of figures below. The first (figure 4.2.2.2.1) demonstrates a randomized muon generation with a net zenith and azimuth angle of trajectory. The second (figure 4.2.2.2.2) demonstrates a muon generated at a vertical initial trajectory at the maximum y-coordinate in the scintillator, to show a maximized differential signal generation between SiPM pairs. Lastly, the third scenario (figure 4.2.2.2.3) shows a dual muon instance. Due to the low sea-level flux of cosmic ray muons and the low surface area of the x-y plane of the scintillator assembly, the assumption is established that dual instances will not occur while a scan is in process.

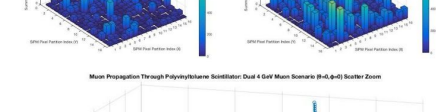
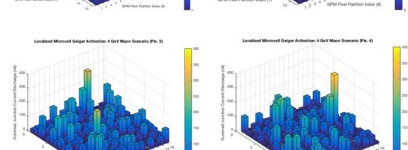
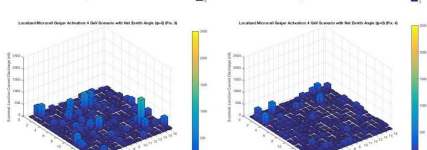
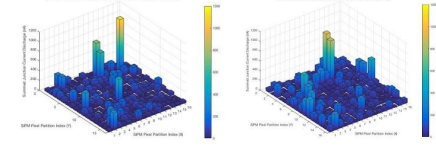
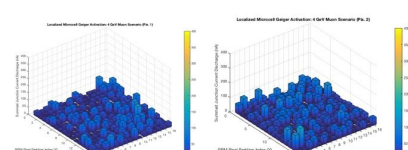
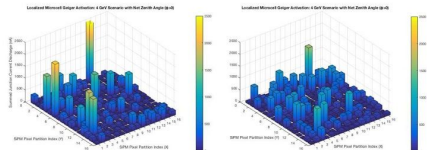
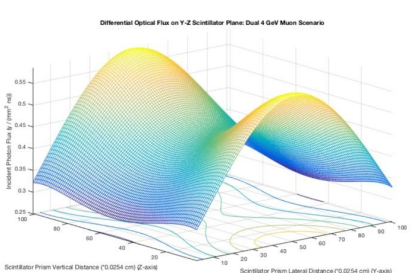
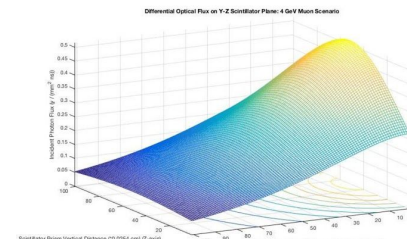
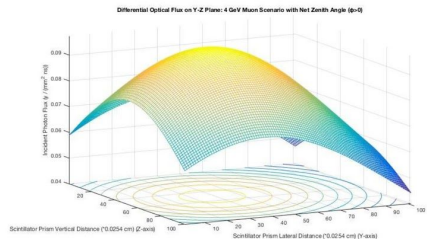
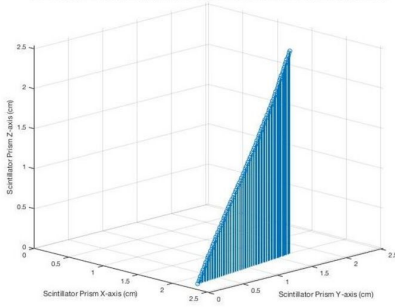
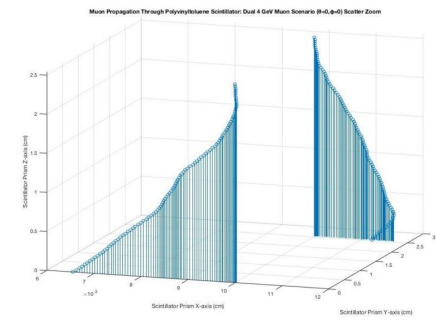
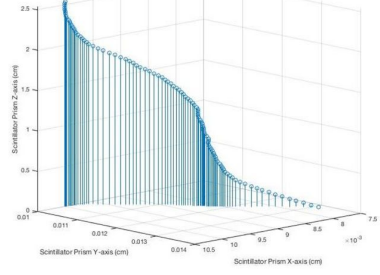
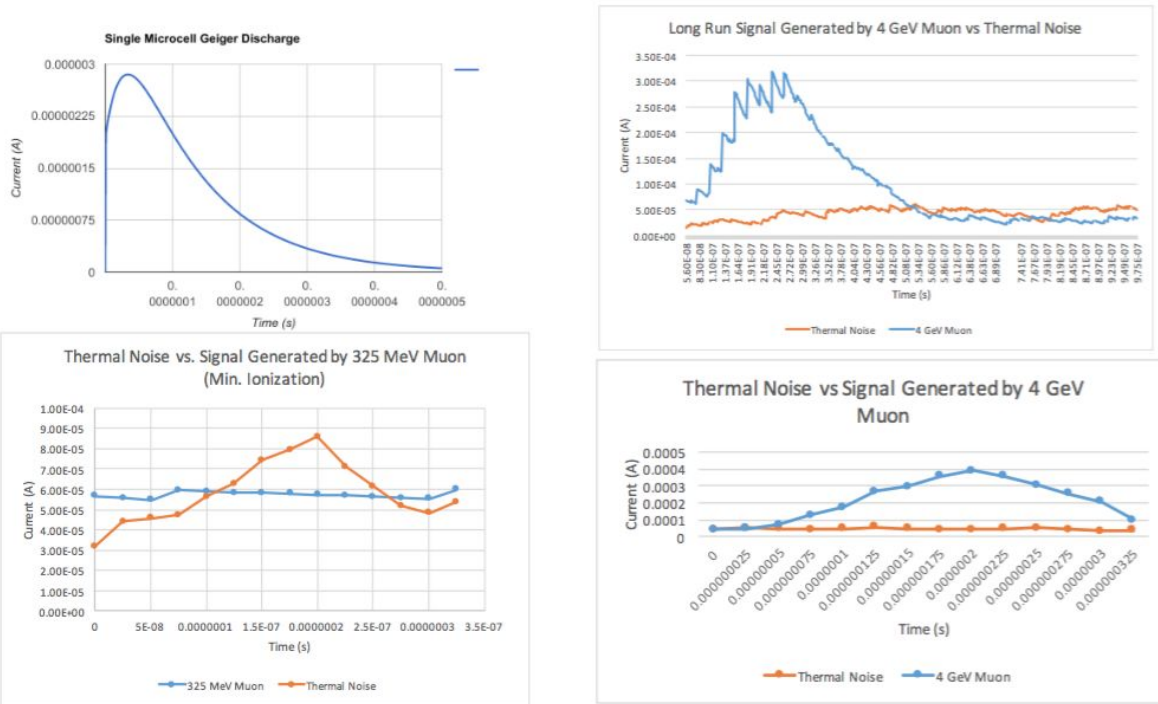
Muon Propagation Through Polyvinyltoluene Scintillator: 4 GeV Muon Scenario ($\theta=0.3925$, $\phi=-0.3164$)Muon Propagation Through Polyvinyltoluene Scintillator: 4 GeV Muon Scenario ($\theta=0.0$, $\phi=0.0$) Scatter Zoom

Figure 4.2.2.2.1. Single [4GeV] muon instance; random zenith, random azimuth, random position.

Figure 4.2.2.2.2. Single [4GeV] muon instance; zero zenith, zero azimuth, start position is maximized in x, y position.

Figure 4.2.2.2.3. Dual [4GeV] muon instance; zero zenith, zero azimuth, opposite extremes of y-axis



Thermal Noise, Crosstalk, and Afterpulsing Simulated Signal

Std. Dev: 1.59E-06

0.00001521394856

Mean: 5.72E-05

0.00005815

2-Sample t-Test: 0.4140454519

The p-value of 0.414 is sufficiently high to fail to reject the assumption that the signal and noise current discharge distributions are equivalent. This merits the use of a peak-detection circuit instead of a raw ADC read-out setup.

Thermal Noise, Crosstalk, and Afterpulsing Simulated Signal

Std. Dev: 0.000005500569448

0.0001210696676

Mean: 0.00004557364286

0.0002129585714

(4.239770802*10^-5 , 4.874957598*10^-5)

(1.430550266*10^-4 , 2.828621154*10^-4)

2-Sample t-Test for 4GeV:

0.00008930948074

4.2.2.3 Voxel resolution

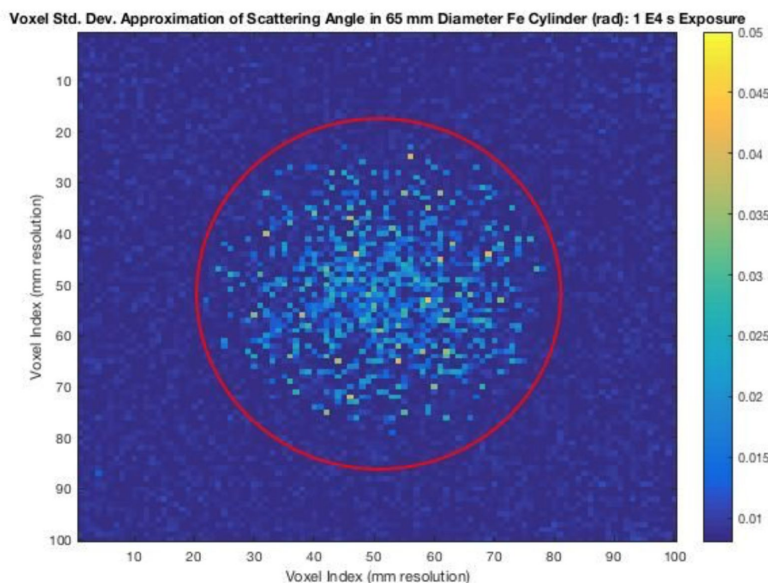


Figure 4.2.2.3.1

Simulation of 65 mm diameter Fe disc situated on polystyrene base. The red annotation above shows the outline of the disc as it appears in the scan field. Successful muon tracking is more frequent towards the center of the disc because the likelihood of the signal coincidence between all four scintillator-SiPM sensing modules is maximized at that position due to net zenith and azimuth angle contributions from the empirical sea-level muon angular distribution. The simulated time exposure is 10,000 seconds, which coupled with the present voxel fill density demonstrates the low rate of data acquisition attributed to the scintillator spacing.

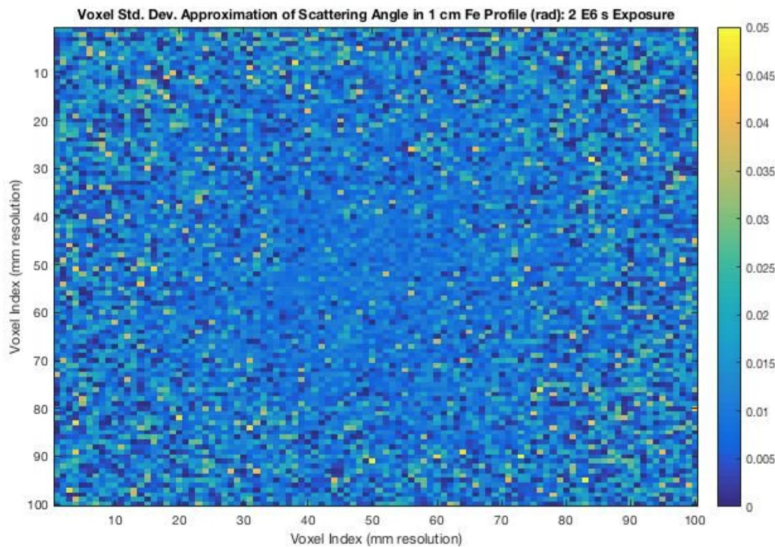


Figure 4.2.2.3.2

Simulation of 1 mm level resolution mapping of sample scan field with randomized muon generation and implementation of trilateration and voxel reconstruction algorithms. The standard deviation of the multiple-Coulomb scattering exhibited by a 960 MeV muon in the 1 cm Fe profile is 0.0106 radians.

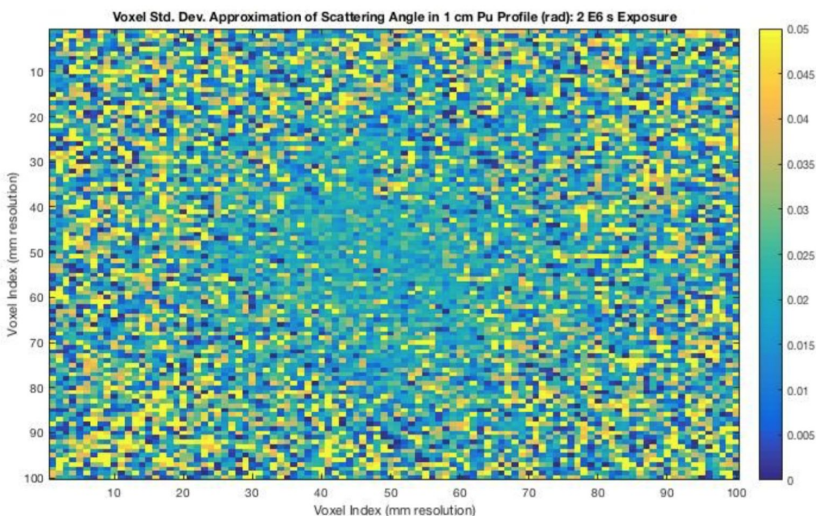


Figure 4.2.2.3.3

Simulation of 1 mm level resolution mapping of sample scan field with randomized muon generation and implementation of trilateration and voxel reconstruction algorithms. The standard deviation of the multiple-Coulomb scattering exhibited by a 960 MeV muon in the 1 cm Pu profile is 0.2256 radians.

5 Conclusion

5.1 Cost efficiency

Compared to typical muon-scattering tomography devices that utilize drift chambers in a six-planar formation, our design only requires three scintillating prismatic planes to measure muon trajectory. In addition, the cost of large plastic scintillators is significantly less than the cost of drift tubes. For instance, the cost of our novel design would be approximately 96.2% less expensive than the recent drift tube implementation outlined in *Tomographic Imaging with Cosmic Ray Muons* (Morris, 2008). Specifically, for an automobile counting station sized 4m x 4m x 5m (Morris, 2008), the traditional cost of 3 million dollars for the six drift tube planes would fall to an estimated \$115,000 using solid-state volumetric scintillators coupled with SiPM arrays.

5.2 Temporal efficiency estimation

According to the Monte Carlo simulation described above which models the temporal efficiency of the prototype design, a cubic millimeter level of voxel resolution (which corresponds to 79,375 z data points) can achieve at least 95% certainty of the mean muon scattering angle and 95% of the scan volume in 41 hours 43 minutes and 31 seconds. This estimate takes into account that 6.23% of the available angular distribution of muons will intersect all 4 scintillators. For the parabolic optical cavity design addendum, it is estimated that the analogous temporal efficiency of an equivalent scan volume and voxel resolution would be 29 minutes and 21 seconds, due to the increase in photon retention as observed by the SiPM array to 83.4% versus a mere 0.58% in the uncladded scintillator concept.

5.3 Performance comparison

After performing a variety of simulation and calibration tests with our design, we can conclude that our novel approach is indeed a cheaper alternative to conventional muon tomography. Our device takes the same scan time to develop a model as other muon tomography devices, while it also provides the same if not better voxel resolution for a far better price.

Comparing the initial trilateration design to the increased PDE version, reveals that investing in a dielectric coating for the device would benefit it. For the parabolic optical cavity scintillator cladded with a dielectric coating to increase overall PDE, the pricing estimate for the milling of the PVT for use on the prototype is \$345, and the anticipated pricing for the application of a MgF₂/TiO₂ dielectric coating is \$1310 for the surface area of 28.18 square centimeters. The ratio of pricing between the parabolic optical cavity design and the uncladded cubic design is 16.07, however the ratio of time efficiencies is 42.53. Therefore, the temporal efficiency to cost ratio of the design addendum is 2.65, meaning that in any application, 2.65 times as many scan volumes may be processed at an equivalent pricing base.

5.4 Limitations in design

The funding for our project was extremely limited which prevented us from building prototypes demonstrating conventional muon tomography designs. The decision was made to invent a more cost

effective method for conducting muon scattering tomography after the proposed scintillating fiber approach was found to be too expensive. There was not enough money to purchase fast readout electronics for muon detection, so additional sample and hold circuitry components had to be examined. In order to save money, all circuitry was constructed at home. When building the physical prototype model, there was no access to professional construction equipment, and various spare parts were found at home and included on the prototype due to lack of funds to purchase more equipment. Pulsing lasers were unavailable to use for calibration testing with the built prototype, so pulsing was improvised using a UV LED and an optical chopper.

5.5 Further research

Further research and testing will be done using operational amplifiers and peak detect circuits. Currently, readout circuitry has been built for one pixel of one SiPM array. After the readout circuits have been built for each pixel, analog to digital conversion will be developed for the purpose of processing muon data into a readable format on a computer. This will make the prototype fully functional and capable of measuring incoming and outgoing muon trajectories to generate tomographic images. Further research into the increased photon detective efficiency design will also be conducted in the near future in order to test the efficacy of the scaled up implementation of our design. Pricing inquiries have been sent to a variety of companies regarding the cost of milling a parabolic scintillator. In addition, the pricing of a dielectric coating applied to a polyvinyl toluene substrate has been investigated. The effectiveness of cooling the SiPMs is being explored in order to reduce dark count rate, since there is a $-0.8\%/\text{C}$ change in gain. Two possible approaches are being examined: the use of a solid-state heat sink such as dry ice, a fluid coolant, or a thermoelectric cooler, which could be more closely modulated. A type-k thermocouple would be used to measure fluctuations in the photomultiplier temperature such that we can closely modify the voltage supply so it accounts for alteration of breakdown voltage with temperature variance.

6 References

Note: All images not explicitly cited herein were created by the authors. Likewise, all numerical statistics not cited explicitly have been developed via the computational methods of the authors.

- 1** SensL. ArrayC PCB Arrays of SiPM User Manual. (2013): 1-35. SensL. Web. Dec. 2016.
- 2** Eljen Technology. Long Decay Time Plastic Scintillator EJ-240 (2016): n. pag. Eljen Technology. Web. Dec. 2016.
- 3** Horowitz, Paul, and Winfield Hill. Feedback and Operational Amplifiers. *The Art of Electronics*. 2nd ed. Cambridge: Cambridge UP, 1989. 1-1125. Print.
- 4** SensL. “Reference Designs for the SMA and SMTPA Boards.” *SMT Board Reference Designs* (2014): 1-15. SensL. Web. Dec. 2016.
- 5** SensL. “An Introduction to the Silicon Photomultiplier.”
- 5** Introduction to SiPM (2011): 1-16. SensL. Web. Dec. 2016.
- 6** Beringer, J., Arguin, J.-F., Barnett, R. M., Copic, K., Dahl, O., Groom, D. E., ... Schaffner, P. “Passage of Particles Through Matter.” *Review of Particle Physics*. By J. Beringer. Vol. 86. N.p.: Particle Data Group, 2013. 1-1637. Web. Dec. 2016.
- 7** Cedex, C. (n.d.). Quenching of Scintillation in for Light Charged Particles Quenching of Scintillation in for Light Charged Particles.
- 8** Coan, T., Liu, T., & Ye, J. (2005). A Compact Apparatus for Muon Lifetime Measurement and Time Dilation Demonstration in the Undergraduate Laboratory. *American Journal of Physics*, 161(2006), 161–164. <https://doi.org/10.1119/1.2135319>
- 9** Hall, R. E., Lind, D. A., & Ristinen, R. A. (1970). A Simplified Muon Lifetime Experiment for the Instructional Laboratory. *American Journal of Physics*. <https://doi.org/10.1119/1.1976002>
- 10** Kruiskamp, M. W., & Leenaerts, D. M. (1994). A CMOS Peak Detect Sample and Hold Circuit. *IEEE Transactions on Nuclear Science*, 41(1), 295–298. <https://doi.org/10.1109/23.281513>
- 11** Liu, L., & Pablo, P. (2007). The Speed and Lifetime of Cosmic Ray Muons, 1–6.
- 12** Morris, C. L., Alexander, C. C., Bacon, J. D., Borozdin, K. N., Clark, D. J., Chartrand, R., ... Blanpied, G. S. (2008). Tomographic Imaging with Cosmic Ray Muons. *Science & Global Security*, 16(1–2), 37–53. <https://doi.org/10.1080/08929880802335758>
- 13** Photodiode, A. (2011). Introduction to the SPM An Introduction to the Silicon Photomultiplier Photon Detection with Silicon Photomultipliers. SensL, 1–8.
- 14** Scheck, F. (1992). Muon physics - Survey. *Zeitschrift F??r Physik C Particles and Fields*, 56(1 Supplement). <https://doi.org/10.1007/BF02426769>
- 15** Seifert, S., Van Dam, H. T., Huizenga, J., Vinke, R., Dendooven, P., Löhner, H., & Schaart, D. R. (2009). Simulation of silicon photomultiplier signals. *IEEE Transactions on Nuclear Science*, 56(6), 3726–3733. <https://doi.org/10.1109/TNS.2009.2030728>
- 16** Tang, A., Horton-Smith, G., Kudryavtsev, V. A., & Tonazzo, A. (2006). Muon simulations for Super-Kamiokande, KamLAND, and CHOOZ. *Physical Review D - Particles, Fields, Gravitation and Cosmology*, 74(5), 1–34. <https://doi.org/10.1103/PhysRevD.74.053007>
- 17** Wright, E. T. (2007).
- 17** A Detector for Muon Tomography : Data Acquisition and Preliminary Results, (May).
- 18** Morris, C (2013). Los Alamos Imaging System, (December 2011).

- 19** Zenoni, A., Bonomi, G., Donzella, A., Subieta, M., Baronio, G., Bodini, I., ... Zumerle, G. (2014). Historical building stability monitoring by means of a cosmic ray tracking system. Retrieved from <http://arxiv.org/abs/1403.1709>
- 20** Sossong, M. J., Us, C. A., & Borozdin, K. N. (2011). (2) Patent Application Publication (10) Pub . No .: US 2011 / 0248163 A1, 1(19).
- 21** Bryman, D., & Classification, P. (2008). (2) Patent Application Publication (10) Pub. No.: US 2008/0128604 A1, 1(19).
- 22** Clarkson, A., Hamilton, D. J., Hoek, M., Ireland, D. G., Johnstone, J. R., Kaiser, R., ... Mahon, D. F. (n.d.). The Design and Performance of a Scintillating-Fibre Tracker for the Cosmic-ray Muon Tomography of Legacy Nuclear Waste Containers.
- 23** Radiology, F., & Engine, I. (n.d.). Radiology Key Cosmic Ray Generated Charged Particles for Cargo Inspection, 3–5.
- 24** Events, U. (n.d.). University of Glasgow. Nuclear Physics Group Muon Tomography Project, 2015, 7–8.
- 25** Jha, Abhinav K., Herman T. Van Dam, Matthew A. Kupinski, and Eric Clarkson. "Simulating Silicon Photomultiplier Response to Scintillation Light." *IEEE Transactions on Nuclear Science* 60.1 (2013): 336-51. Web.
- 26** Straten, Peter Van Der, and Harold J. Metcalf. *Atoms and Molecules Interacting with Light: Atomic Physics for the Laser Era*. Cambridge: Cambridge UP, 2016. Print.
- 27** "Muon Basics." National University of La Plata, n.d. Web. 13 May 2017.
- 28** Kuo, Yi-Hong. *Determination of the Angular Distribution of Cosmic Rays at Sea Level*. Thesis. Massachusetts Institute of Technology, 2010. N.p.: n.p., 2010. Print.
- 29** Gnanvo, K., Benson, B., Bittner, W., Costa, F., Grasso, L., Hohlmann, M., ... Toledo, J. (2010). Detection and Imaging of High-Z Materials with a Muon Tomography Station Using GEM Detectors.
- 30** Blum, W., Riegler, W., & Rolandi, L. (2010). *Particle detection with drift chambers*. Berlin: Springer-Verlag.
- 31** Rossi, B. (1948). *Interpretation of cosmic ray phenomena*. Cambridge, MA: Massachusetts Institute of Technology.
- 32** Paschotta, Dr. Rüdiger. "Dielectric Mirrors." *Encyclopedia of Laser Physics and Technology - Dielectric Mirrors, Laser Mirrors, Thin-film Coating, Multilayer, Mirror Design, Fabrication*. N.p., 29 Mar. 2017. Web. 13 May 2017.
- 33** Max Planck Institute for Nuclear Physics. (n.d.). Cosmic ray research.